

POLITECNICO DI TORINO

Master's Degree in Aerospace Engineering



Master's Degree Thesis

Guidance and control strategies for a 12U CubeSat involved in the observation/inspection of a collaborative target

Supervisors

Prof. Fabrizio STESINA

Eng. Antonio D'ORTONA

Candidate

Leonardo PAPPALARDO

April 2023

Abstract

The development of technologies that enable operational capabilities that broaden the range of missions carried out by CubeSats has recently been the focus of governmental and private actors in the field of small satellites. The examination and observation of larger spacecraft (like the International Space Station) or debris is a useful example of a new small-sat mission. In this context, a TDE study developed the Space Rider Observer Cube (SROC) mission, which attempts to demonstrate the critical capabilities and technologies needed to successfully carry out an inspection mission in a safety-sensitive environment. This in-orbit demonstration could pave the way for a variety of cutting-edge CubeSat applications in the field of inspection missions. Space Rider is an unmanned spacecraft designed to provide Europe routine access and return from Low-Earth Orbit (LEO) with a space transportation system that is economical, independent, and reusable. The SROC mission consists of a 12U CubeSat deployed from the Space Rider cargo bay to closely inspect the vehicle in a safety-sensitive context with a multispectral camera. In fact, visual, near-infrared, and thermal infrared photos of Space Rider in-orbit may be useful for understanding its status and performance (e.g. heat shield deterioration), as well as for outreach. The main objective of the thesis is to define guidance and control strategies for small satellites involved in the observation/inspection of a collaborative target. Due to the difficulties in modeling internal and external disturbances and usually also in accurately measuring the system parameters, a super-twisting sliding mode control law has been proposed for the spacecraft attitude tracking. For the attitude guidance it has been used a method based on computing the Euler axis to correctly point, in each position of the trajectory, to the center of mass of Space Rider. Then, in MATLAB and Simulink environment, it has been implemented an orbital simulator where the attitude dynamics and the attitude control could be simulated. Finally, a robustness analysis through Monte Carlo simulations has been conducted.

Acknowledgements

Grazie a chi conosco da sempre, a chi conosco dal primo giorno e a chi ho conosciuto lungo il percorso che mi ha condotto fino a qui. Grazie perché tutti voi, in modo più o meno determinante, mi avete aiutato ad arrivare fino a qui.

Grazie a mamma e papà, che hanno sempre creduto in me e che mi hanno permesso di iniziare e terminare i miei studi.

Grazie a mia sorella Gaia, che dipinge le mie giornate con la sua simpatia e naturalezza.

Grazie a nonno Fernando per essere un tale esempio. Spero un giorno di poter affermare di essere diventato almeno la metà di quello che sei stato e sei per me.

Grazie a nonna Rita che, nella sua semplicità, mi ha insegnato cosa sono i veri valori della vita. Grazie ovviamente anche per chiedermi ancora come sta andando a scuola e per avermi aiutato con la tesi (probabilmente non l'avrei finita senza di te).

Grazie a nonna Melina, probabilmente la donna più forte che io conosca. Grazie per avermi sempre nutrito con le giuste calorie durante le vacanze, permettendomi di studiare e continuare la tesi.

Grazie a zio Walter, zia Paola, Rocco e Giulio per essermi stati vicini come se abitassero a 600 m di distanza (invece che 600 km).

GRAZIE

Table of Contents

List of Tables	VI
List of Figures	VII
1 Introduction	1
2 Mathematical problem	5
2.1 Manoeuvre description	5
2.2 Control laws	7
2.2.1 Sliding Mode Control (SMC)	7
2.2.2 Output Tracking: Conventional Sliding Mode Controller Design	15
2.2.3 Super-Twisting SMC	17
3 Solutions	21
3.1 Helix manoeuvre	21
3.2 Attitude guidance	25
3.3 Attitude control with Super-Twisting SMC	31
4 Mathematical model and simulations	33
4.1 Mathematical model	33
4.1.1 SROC attitude dynamics and kinematics	33
4.1.2 Reaction Wheels model	35
4.1.3 External disturbances	36
4.2 Simulations	39
4.2.1 Nominal scenario	41
4.2.2 Robustness analysis	41
4.2.3 Off-nominal scenario	43
5 Results and discussions	44
5.1 Nominal scenario	44
5.1.1 Helix manoeuvre (3.3)	44

5.1.2	Helix manoeuvre (3.4)	55
5.2	Monte Carlo simulation: nominal scenario	66
5.3	Monte Carlo simulation: off-nominal scenario	70
6	Model Predictive Control	74
6.1	Constrained LQ Finite Horizon optimal control	74
6.2	Tracking MPC	76
6.3	MPC for tracking attitude control	77
6.4	Simulations and results	78
7	Conclusions	82
A	Reference frames	83
A.1	Earth centered inertial frame	83
A.2	Body reference frame	84
A.3	LVLH frame	84
B	Euler angles	85
C	Quaternions	88
C.1	Euler's axis rotation theorem	88
C.2	The quaternion error vector	89
D	Impulsive manoeuvres	91
D.1	Radial boost	91
D.2	Motion in the y direction	93
	Bibliography	94

List of Tables

4.1	Control gains for the simulations of the Helix manoeuvre (3.3) . . .	41
4.2	Control gains for the simulations of the Helix manoeuvre (3.4) . . .	41
4.3	Minimum number of simulation runs required to verify a requirement at confidence level P_c [37]	42
4.4	Initial conditions of the simulation with the boundaries of uncertainties	43
5.1	Initial conditions of the simulation	44
5.2	Initial conditions of the simulation	52
5.3	Case 1: <i>APE</i> , <i>MPE</i> and <i>RPE</i>	54
5.4	Case 2: <i>APE</i> , <i>MPE</i> and <i>RPE</i>	54
5.5	Initial conditions of the simulation	55
5.6	Initial conditions of the simulation	63
5.7	Case 1: <i>APE</i> , <i>MPE</i> and <i>RPE</i>	65
5.8	Case 2: <i>APE</i> , <i>MPE</i> and <i>RPE</i>	65

List of Figures

2.1	Helix manoeuvre	6
2.2	Sliding manifold [33]	8
2.3	Single-dimensional motion of a unit mass [9]	9
2.4	Asymptotic convergence for $f(x_1, x_2, t) = 0$ [9]	10
2.5	Convergence to the domain Ω for $f(x_1, x_2, t) = \sin(2t)$ [9]	10
2.6	Sliding variable [9]	13
2.7	Asymptotic convergence for $f(x_1, x_2, t) = \sin(2t)$ [9]	13
2.8	Phase portrait [9]	14
2.9	Phase portrait (zoom) [9]	15
2.10	The reference profile tracking [9]	17
2.11	Sliding variable σ [9]	19
2.12	The reference profile tracking [9]	20
2.13	Super-twisting control [9]	20
2.14	Time history of $\text{sign}(\sigma)$ [9]	20
3.1	Helix manoeuvre (3.3) in four orbital periods	22
3.2	Helix manoeuvre (3.4) in four orbital periods	23
3.3	Focus of the Helix manoeuvre represented in Fig. 3.2	24
3.4	$x - z$ plane of the Helix manoeuvre (3.3) ($x_0 = -1950$ m, $y_0 = -200$ m and $z_0 = 0$ m)	26
3.5	$x - y$ plane of the Helix manoeuvre (3.3) ($x_0 = -1950$ m, $y_0 = -200$ m and $z_0 = 0$ m)	26
3.6	$x - z$ plane of the Helix manoeuvre (3.3) ($x_0 = -2050$ m, $y_0 = -200$ m and $z_0 = 0$ m)	27
3.7	$x - y$ plane of the Helix manoeuvre (3.3) ($x_0 = -2050$ m, $y_0 = -200$ m and $z_0 = 0$ m)	28
3.8	Euler's axis in a generic point of the trajectory	30
4.1	GNC functions [35]	34
4.2	4 Reaction Wheels in a pyramidal configuration [33]	36
4.3	Simple gravity gradient torque example [32]	38

4.4	Orbital simulator architecture	40
5.1	Helix manoeuvre (3.3) in four orbital periods (Table 5.1)	45
5.2	Temporal evolution of q_0 during tracking attitude control (Table 5.1)	46
5.3	Temporal evolution of q_1 during tracking attitude control (Table 5.1)	47
5.4	Temporal evolution of q_2 during tracking attitude control (Table 5.1)	47
5.5	Temporal evolution of q_3 during tracking attitude control (Table 5.1)	48
5.6	Temporal evolution of the quaternion error during tracking attitude control (Table 5.1)	49
5.7	Temporal evolution of the angular velocity error during tracking attitude control (Table 5.1)	50
5.8	Zoom of Fig. 5.5	51
5.9	Helix manoeuvre (3.3) in four orbital periods (Table 5.2)	52
5.10	Temporal evolution of q_0 during tracking attitude control (Table 5.2)	53
5.11	Temporal evolution of q_1 during tracking attitude control (Table 5.2)	53
5.12	Temporal evolution of q_2 during tracking attitude control (Table 5.2)	53
5.13	Temporal evolution of q_3 during tracking attitude control (Table 5.2)	53
5.14	Temporal evolution of the quaternion error during tracking attitude control (Table 5.2)	54
5.15	Temporal evolution of the angular velocity error during tracking attitude control (Table 5.2)	54
5.16	Helix manoeuvre (3.4) in four orbital periods (Table 5.5)	56
5.17	Temporal evolution of q_0 during tracking attitude control (Table 5.5)	57
5.18	Temporal evolution of q_1 during tracking attitude control (Table 5.5)	58
5.19	Temporal evolution of q_2 during tracking attitude control (Table 5.5)	59
5.20	Temporal evolution of q_3 during tracking attitude control (Table 5.5)	60
5.21	Temporal evolution of the quaternion error during tracking attitude control (Table 5.5)	61
5.22	Temporal evolution of the angular velocity error during tracking attitude control (Table 5.5)	62
5.23	Helix manoeuvre (3.4) in four orbital periods (Table 5.6)	63
5.24	Temporal evolution of q_0 during tracking attitude control (Table 5.6)	64
5.25	Temporal evolution of q_1 during tracking attitude control (Table 5.6)	64
5.26	Temporal evolution of q_2 during tracking attitude control (Table 5.6)	64
5.27	Temporal evolution of q_3 during tracking attitude control (Table 5.6)	64
5.28	Temporal evolution of the quaternion error during tracking attitude control (Table 5.6)	65
5.29	Temporal evolution of the angular velocity error during tracking attitude control (Table 5.6)	65
5.30	Maximum Absolute Performance Error (APE) over the 58 Monte Carlo simulations	66

5.31	Mean Performance Error (MPE) over the 58 Monte Carlo simulations	67
5.32	Relative Performance Error (RPE) over the 58 Monte Carlo simulations	68
5.33	RWs mean torques T_{mean} over the 58 Monte Carlo simulations . . .	69
5.34	Maximum Absolute Performance Error (APE) over the 120 Monte Carlo simulations	70
5.35	Mean Performance Error (MPE) over the 120 Monte Carlo simulations	71
5.36	Relative Performance Error (RPE) over the 120 Monte Carlo simulations	72
5.37	RWs mean torques T_{mean} over the 120 Monte Carlo simulations . . .	73
6.1	Temporal evolution of q_0 during tracking attitude control	80
6.2	Temporal evolution of q_1 during tracking attitude control	80
6.3	Temporal evolution of q_2 during tracking attitude control	81
6.4	Temporal evolution of q_3 during tracking attitude control	81
A.1	Earth inertial frame [41]	83
A.2	LVLH frame [33]	84
C.1	Euler's axis rotation theorem [33]	88
D.1	Transfer along V-bar byradial impulses [35]	92
D.2	Motion over time after release at an out-of-plane distance of $Y_0 = 10\text{ m}$ [35]	93

Chapter 1

Introduction

In their surroundings, satellites are singularly alone. From initial operational capability (IOC) to end of life, they are launched with everything they require for their entire mission. With the October 4, 1957 launch of Sputnik, this has been the standard in civil, commercial, and military spacecraft design. This eventually produced fully redundant designs and extremely lengthy mission life. Satellites cannot currently be physically upgraded, refueled, or repaired after they are in orbit, with a few notable exceptions. On-orbit servicing (OOS) activities, however, have only sometimes been carried out since the beginning of space exploration. Gemini and Apollo missions managed to demonstrate rendezvous and proximity maneuvers (RPO). Skylab and Solar Maximum Mission (SMM) showed that it was possible to repair essential components while in orbit, with SMM utilizing a modular design and orbital replacement units (ORUs). Five service visits were made to the Hubble Space Telescope (HST), during which time circuit boards were replaced. The International Space Station (ISS) was built in space and is continuously upgraded with new modules, supplies, and fuel to expand its capabilities and open up new scientific opportunities. All of these tasks required the involvement of humans, either directly or indirectly. However, the Orbital Express (OE) by the Defense Advanced Research Projects Agency (DARPA) demonstrated a full end-to-end robotic satellite servicing mission that featured autonomous docking, fuel transfer, and ORU change-out, basically taking humans out of the picture.

OOS refers to on-orbit operations carried out by a spacecraft that closely examines another resident space object (RSO) or causes intentional and positive alterations to that item. Non-contact support, orbit modification (relocation), maintenance, refueling and supplies replenishment, upgrade, repair, assembly, and debris mitigation are some of these tasks. A servicer is a spacecraft with equipment intended solely for doing servicing activities. Client refers to an RSO that has received OOS. A customer may be cooperative or uncooperative. Information (position, velocity, health/status, etc.) is transferred between the servicer and client

via two-way crosslinks or ground connections to facilitate tasks like as acquisition, tracking, rendezvous, mating, and/or servicing. A commercial resupply vehicle made to mate with the ISS is an illustration of a cooperative client. A non-cooperative client does not provide information with the servicer and does not provide features intended to facilitate acquisition, tracking, rendezvous, mating, and/or servicing activities. Examples of uncooperative customers include defunct satellites, abandoned rocket bodies, and orbital debris. The level of cooperability is a spectrum, and most of the time a client is neither fully cooperative nor uncooperative.

In this context, one of the most relevant planned mission is the Space Rider Observer Cube (SROC) mission, which aims to demonstrate the critical capabilities and technologies required for successfully executing an inspection mission in a safety-sensitive context. This in-orbit demonstration has the potential to open a wide spectrum of novel applications for CubeSats in the area of inspection missions. In fact, the close observation of orbiting objects with Cubesats can efficiently support a wide range of applications, such as the inspection of defunct satellites for preparing active debris removal missions, or the inspection of operative spacecraft (International Space Station, telecom satellites) for maintenance purposes. Multispectral images (visual, near-infrared, thermal infrared) of Space Rider (SR) in-orbit could be beneficial for getting insight in its performance and status (e.g. heat shield degradation), and for outreach purposes. The SROC Design Reference Mission consists of a 12U CubeSat deployed from the Space Rider cargo bay with the purpose of imaging the vehicle from its vicinity with a multispectral camera. The main objective of the thesis is to define guidance and control strategies for 12U Cubesat involved in the observation/inspection of a collaborative target; in particular, SROC has to point the center of mass of Space Rider during all the manoeuvre.

Due to the constrained hardware resources of the sensors, actuators, and processors installed on board, precise attitude tracking control of small satellites is a challenging issue. The attitude control of miniaturized spacecraft is further complicated by the impact of model uncertainty and persistent disturbances like gravity-gradient, magnetic, aerodynamic, and solar radiation pressure torques on the satellite dynamics. Hence, robust controllers represent a more dependable solution to cope with the mission limits when actuator limitations and strict pointing requirements exist.

In recent years, Sliding Mode Control (SMC) techniques, such as adaptive Super-Twisting SMC [1, 2], fractional-order Sliding Mode Control [3], finite time control [4], robust backstepping SMC [5, 6, 7], and Model Predictive SMC [8], have become a major research area in control theory. One of the characteristics of the SMC is its better resistance to matching disturbances. The chattering effect of the control signal is the cost of robustness, though. For actual implementations, it

makes application challenging [9]. The following are some strategies to reduce the chattering phenomenon [10, 11, 12]:

1. substituting a saturation function or sigmoid function for the discontinuous switching function;
2. employing an adaptive law to dynamically change the switching gain;
3. utilizing higher-order SMC approaches.

Yet, skill (1) causes the robustness to the disturbances to be lost. Despite the fact that technique (2) can estimate the switching gain's magnitude accurately in relation to perturbations [13, 14], the estimation of the switching gain may rise monotonically because there isn't always ideal sliding motion in real-world applications. The gain/stability calculations for (3) are rather difficult. In the presence of the matched perturbations, the high-order SMC method can drive the sliding variable and its subsequent derivations to zero. However, the fact that the high-order SMC relies on data from the high-order temporal derivatives of the sliding variable presents its primary difficulty [15, 16]. The second-order SMC, like the Super-Twisting algorithm, among the higher-order SMC algorithms, should be noted as requiring only the feedback data of the sliding variable in the control process. Dr. Levant made the initial Super-Twisting algorithm proposal [17]. In the proof of the finite-time convergence property, a quadratic Lyapunov function suggested in [18] is taken into account. The Super-Twisting method has been used in numerous investigations, including quadrotor [19, 20], industrial emulator [21], and mobile wheeled inverted pendulum [22], due to its better features. While [23] suggests a modified form of Linear Matrix Inequality (LMI) that can meet the convergence performance by requirement and has more degrees of freedom for determining the decision variables, [24] develops a Super-Twisting Sliding Mode Control to provide precise attitude tracking for a flexible spacecraft's attitude and suppress the exciting vibration of its appendages at the same time. For this reason, in this thesis the robust continuous Super-Twisting Sliding Mode algorithm will be used for the attitude tracking control.

Furthermore, an other reliable solution may be the Model Predictive Control (MPC), even though it is usually necessary to linearize the attitude dynamics (resulting in simplifications in neglecting the non-linearities). In fact, Model Predictive Control has been used in spacecraft relative motion and attitude control as a successful feedback control technique that resolves an online constrained optimization problem [25, 26]. While non-linear dynamics and constraints would necessitate the use of a non-linear MPC (NMPC) [27], unless the problem is linearized, such as rotating hyperplanes [28, 29], the optimization problem can be reduced to a constrained quadratic programming (QP) problem when MPC is applied to linearized dynamics with linear constraints. However, classical MPC

controllers can only provide a limited degree of inherent robustness as a feedback control scheme, which makes them insufficient to ensure the robustness needed to deal with disturbances and to satisfy mission and system constraints when external noise is present in the system dynamics [30]. Hence, a robust method is necessary to ensure performance under nominal operating conditions as well as to provide adequate resilience against parametric uncertainty and persistent disruption. For this reason, [31] proposes a tube-based robust MPC (TRMPC) approach to control the attitude of a small satellite during an Earth observation mission in order to guarantee the desired pointing accuracy. Moreover, [32] suggests a TRMPC for accurate attitude control that is based on quaternion error linearized attitude dynamics. In this context, in the chapter 6 of this thesis a Model Predictive Control algorithm for the attitude tracking control in the case of a time-varying reference will be introduced.

Chapter 2

Mathematical problem

2.1 Manoeuvre description

Once the deployment from the Space Rider cargo bay, the Early Operations Phase (EOP) and the Rendezvous Phase are completed, SROC achieves the relative position with respect to Space Rider to start the Observation Phase; during this phase, the manoeuvre, that SROC has to carry out, can be summarized as follows: SROC performs 4 ellipses (with a radius of about 200 m) around Space Rider advancing along the x direction in the LVLH frame (Appendix A) and guaranteeing the payload operating range.

The figure 1 shows an example of the manoeuvre in the LVLH frame centered on Space Rider.

Therefore, the objective is to define an attitude guidance, based on the Euler Angles (Appendix B) or on the quaternions (Appendix C), in order to ensure that SROC, in every point of its trajectory, can point to Space Rider's center of mass. Once an attitude guidance is defined, it is necessary to select the most suitable control law. It is evident that the case analysis is a problem of non-linear attitude control, therefore it is not possible to choose any kind of control law because, for example, the PID controller requires a linear dynamic system or non-linear dynamic system that can be linearized around an equilibrium point. Furthermore, the system mathematical model is often difficult to model due to the presence of non-linearities, which should be neglected, variables or other simplifications, these models are not always reliable. Beside these motivations some dynamic phenomena could be neglected and, at the same time, a perfect evaluation of disturbances is impossible. Robustness is required to design a system through strong simplifications. Therefore, also the Linear Quadratic Regulator (LQR) controller is not suitable for the case analysis, because it is robust with respect to only small uncertainties.

According to all these considerations, the most suitable control laws that have

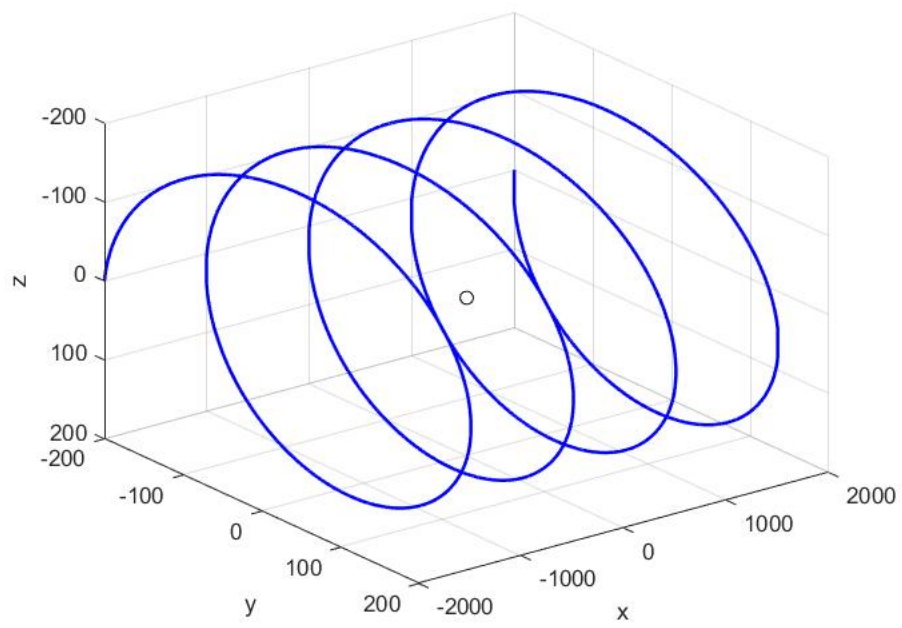


Figure 2.1: Helix manoeuvre

been selected are the Sliding Mode Control (SMC) and the Model Predictive Control (MPC).

2.2 Control laws

2.2.1 Sliding Mode Control (SMC)

The area of mathematics and engineering known as control theory investigates how dynamical systems behave when their parameters are time-varying. The goal of automated control is to alter input variables so that a command input can alter the system's behavior. A set of first differential equations can adequately describe any dynamic system with a finite dimension.

There will always be a disparity between the real plant and its mathematical model employed for controller design in the creation of any practical control challenge. When neglected parameters and outside disruptions are added, these differences become more pronounced. The goal of the theory of Sliding Mode Control and other robust controls is to address this issue. Moreover, systems are sometimes approximated as linear around an equilibrium point, ignoring non-linearities, but since SMC is a non-linear control, this is not a source of mistakes. So, the primary benefit of Sliding Mode is its low sensitivity to changes in plant parameters and disturbances, which minimizes the need for precise modeling. Theoretically, even in the presence of disruptions and model flaws, the system will always remain in those settings once it reaches the Sliding Surface. By introducing a control signal at an intermittent frequency, these optimal circumstances are maintained. In the real scenario, the system trajectory oscillates around to the Sliding Surface (chattering), and the width of the fluctuation is inversely proportional to the frequency.

The SMC approach is the following:

1. A so-called sliding surface is defined; this surface is a subset of the state space, on which the trajectory of the plant is desired to lie
2. A feedback law is designed to bring the plant trajectory towards the sliding surface and, once there, to stay close to this surface.

Considering a generic nonlinear dynamical system described by its state equation

$$\dot{x}(t) = f(x(t), u(t))$$

Where $x(t) \in R^n$ is the system state and $u(t) \in R^{n_u}$ is the system input (control input).

Considering a function of the state system, named sliding variable

$$\sigma(x(t)) \in R^m$$

and the associated, manifold named sliding manifold

$$\sigma(x(t)) = 0$$

The sliding manifold is a subspace of the system state space having dimension n, m and it can be a single surface or be given by the intersection of several surfaces. When the state trajectory continuously crosses the sliding manifold, since in its vicinity the state motion is always directed towards the manifold, a sliding mode is enforced.

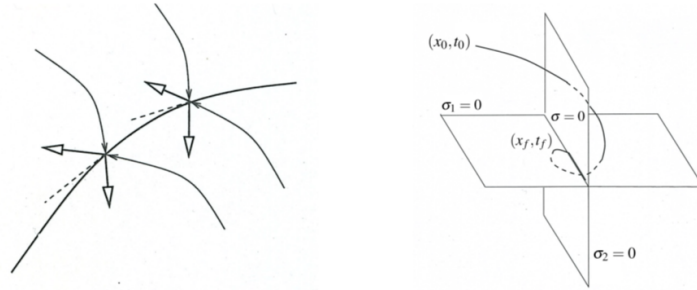


Figure 2.2: Sliding manifold [33]

Therefore, two elements need to be “designed”:

1. The sliding manifold: it is designed so that the system in sliding mode evolves in the desired way (e.g. it results in being linearized and its state is asymptotically regulated to zero, or it satisfies some optimality requirement, etc.)
2. The control law: it has to be chosen in order to enforce a sliding mode [33].

The main advantages of sliding mode control, including robustness, finite-time convergence, and reduced-order compensated dynamics, are demonstrated on numerous examples and simulation plots.

For example, a single-dimensional motion of a unit mass is considered in fig. (2.3).

A state-variable description is obtained by introducing variables for the position $x_1 = x$ and the velocity $x_2 = \dot{x}_1$ so that

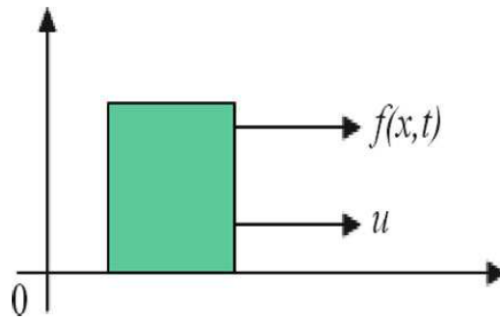


Figure 2.3: Single-dimensional motion of a unit mass [9]

$$\begin{cases} \dot{x}_1 = x_2 \\ \dot{x}_2 = u + f(x_1, x_2, t) \end{cases} \quad (2.1)$$

Where u is the control force and $f(x_1, x_2, t)$ is the disturbance term. The problem is to design a feedback control law $u = u(x_1, x_2)$ that drives the state variables to zero: i.e. $\lim_{t \rightarrow \infty} x_1, x_2 = 0$. For instance, [9] proposes a linear state-feedback control law

$$u = -k_1 x_1 - k_2 x_2, \quad k_1 > 0, k_2 > 0 \quad (2.2)$$

that provides asymptotic stability of the origin only for $f(x_1, x_2, t) = 0$ (Fig. 2.4) and typically only drives the states to a bounded domain $\Omega(x_1, x_2, L)$ for $|f(x_1, x_2, t)| \leq L > 0$ (Fig. 2.5)

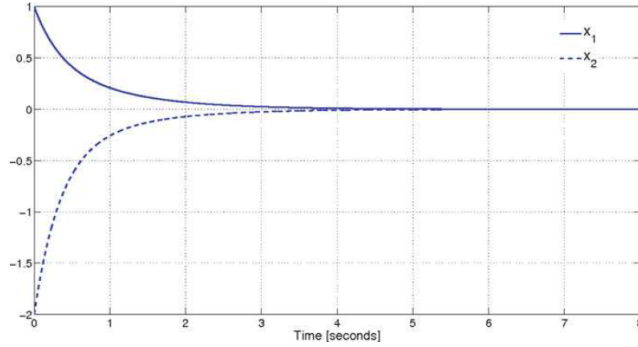


Figure 2.4: Asymptotic convergence for $f(x_1, x_2, t) = 0$ [9]

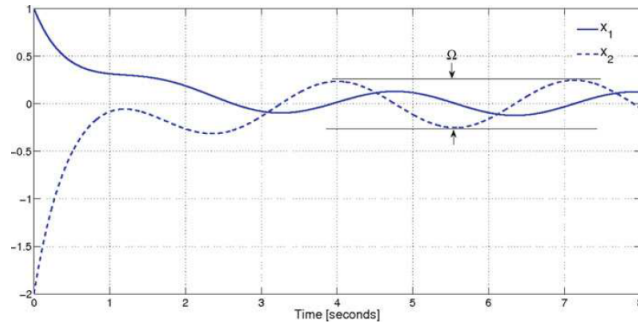


Figure 2.5: Convergence to the domain Ω for $f(x_1, x_2, t) = \sin(2t)$ [9]

A new variable in the state space of the system is introduced [9]

$$\sigma = \sigma(x_1, x_2) = x_2 + cx_1, \quad c > 0 \quad (2.3)$$

In the presence of the bounded disturbance $f(x_1, x_2, t)$, it is necessary to drive the variable σ to zero in finite time using the control u in order to accomplish asymptotic convergence of the state variables to zero. This task can be achieved by applying Lyapunov function techniques to the σ -dynamics that are derived using (2.1) and (2.3)

$$\dot{\sigma} = cx_2 + f(x_1, x_2, t) + u \quad (2.4)$$

For the σ -dynamics (2.4) a candidate Lyapunov function (Appendix) is introduced taking the form [9]

$$V = \frac{1}{2}\sigma^2 \quad (2.5)$$

In order to provide the asymptotic stability of Eq. (2.4) about the equilibrium point $\sigma = 0$, the following conditions must be satisfied:

1. $\dot{V} < 0$ for $x \neq 0$
2. $\lim_{|\sigma| \rightarrow \infty} V = \infty$

Condition (2) is satisfied by V in Eq. (2.5). In order to achieve finite-time convergence (global finite-time stability), condition (a) can be modified to be

$$\dot{V} \leq -\alpha V^{1/2}, \quad \alpha > 0 \quad (2.6)$$

Indeed, separating variables and integrating inequality (2.6) over the time interval $0 \leq \tau \leq t$, $V(t)$ reaches zero in a finite time t_r that is bounded by

$$t_r \leq \frac{2V^{1/2}(0)}{\alpha} \quad (2.7)$$

As a result, a control u , that is calculated to fulfill Eq. (2.6), will eventually drive the variable to zero and keep it there. The derivative of V is computed as

$$\dot{V} = \sigma \dot{\sigma} = \sigma(cx_2 + f(x_1, x_2, t) + u) \quad (2.8)$$

Selecting $u = -cx_2 - \rho \text{sign}(\sigma)$ where

$$\text{sign}(\sigma) = 1, \text{ if } \sigma > 0$$

$$\text{sign}(\sigma) = -1, \text{ if } \sigma < 0$$

and substituting it into Eq. (2.8)

$$\dot{V} = (x_1, x_2, t) + \sigma(-\rho \text{sign}(\sigma)) \leq |\sigma|L - |\sigma|\rho \quad (2.9)$$

Taking into account Eq. (2.5), condition (2.6) can be rewritten as

$$\dot{V} \leq -\alpha V^{1/2} = -\frac{\alpha}{\sqrt{2}}|\sigma| \quad (2.10)$$

Combining Eqs. (2.9) and (2.10)

$$\dot{V} \leq -|\sigma|(\rho - L) = -\frac{\alpha}{\sqrt{2}}|\sigma| \quad (2.11)$$

Finally, the control gain ρ is

$$\rho = -\frac{\alpha}{\sqrt{2}} \quad (2.12)$$

Consequently a control law u that drives σ to zero in finite time (2.7) is

$$u = -cx_2 - \rho \text{sign}(\sigma) \quad (2.13)$$

The sliding surface reaching time specified by Eq. (2.7) is determined by the second term of the control gain, whereas the bounded disturbance $f(x_1, x_2, t)$ is compensated for by the first component of the control gain. The larger α , the shorter the reaching time. Finally, the variable (2.3) is called a sliding variable, $\sigma = x_2 + cx_1$ is called sliding surface or sliding manifold.

Figure 2.6 shows how the sliding variable eventually converges to zero in finite time. Fig. 2.7 depicts the state variables x_1 and x_2 asymptotically convergent to zero in the presence of the external bounded disturbance $f(x_1, x_2, t) = \sin(2t)$. A reaching phase occurs when the state trajectory is pushed towards the sliding surface, and a sliding phase occurs when the state trajectory is going toward the origin along the sliding surface, as shown by the phase portrait in Fig. 2.8.

The "zigzag" motion of small amplitude and high frequency that the state variables display while in the sliding mode is depicted in a zoomed area of the phase portrait Fig. 2.8. Sliding mode control is a high frequency switching control

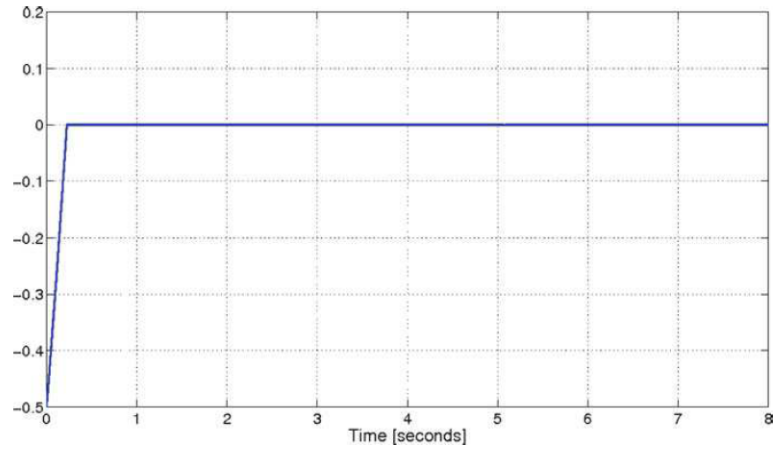


Figure 2.6: Sliding variable [9]

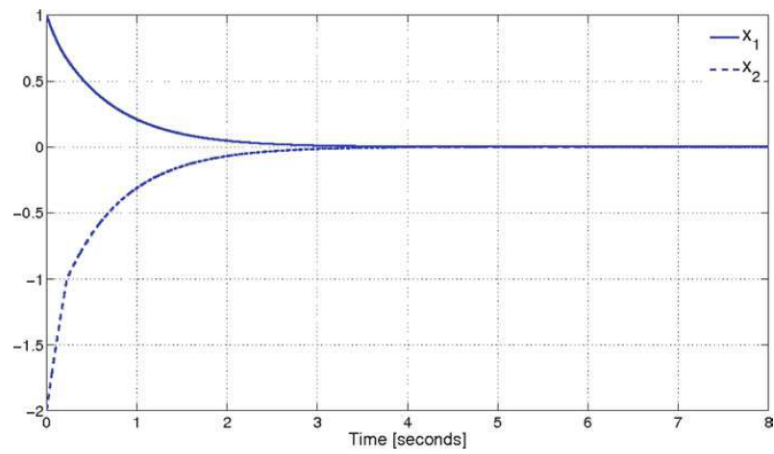


Figure 2.7: Asymptotic convergence for $f(x_1, x_2, t) = \sin(2t)$ [9]

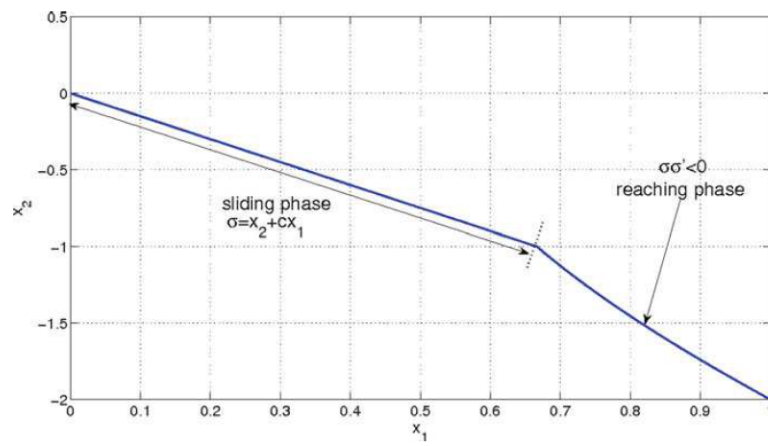


Figure 2.8: Phase portrait [9]

with a switching frequency inversely proportional to the time increment used in the simulation. Apparently, this high-frequency switching control causes the “Zigzag” motion in the sliding mode (Fig. 2.9). In an ideal sliding mode the switching frequency is supposed to approach infinity and the amplitude of the “zigzag” motion tends to zero. As it is possible to see in Fig. 2.9 and, the imperfection in the sign-function implementation yields a finite amplitude and finite frequency “zigzag” motion in the sliding mode due to the discrete-time nature of the computer simulation. This effect is called chattering [9].

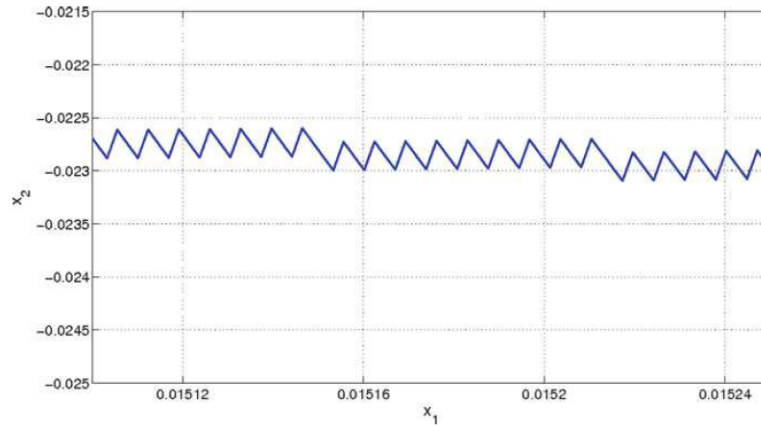


Figure 2.9: Phase portrait (zoom) [9]

2.2.2 Output Tracking: Conventional Sliding Mode Controller Design

The control problem of the output tracking (servomechanism) is a fairly frequent task in practice. By controlling the deflection of the aerodynamic surfaces, an aircraft flight control system, for example, makes the aircraft attitude (Euler) angles follow reference profiles that are frequently generated in real time, while the state vector linked to the aircraft dynamics contains a number of other variables that are under control. In this way, it is possible to review the system (2.1):

$$\begin{cases} \dot{x}_1 = x_2 \\ \dot{x}_2 = u + f(x_1, x_2, t) \\ y = x_1 \end{cases} \quad (2.14)$$

where y is a controlled output. Now it is necessary to design an SMC control law $u = u(x_1, x_2, t)$ that makes the output y (the position of the unit mass) follow

asymptotically a reference profile $y_c(t)$ given in current time. In other words, the control $u = u(x_1, x_2, t)$ is supposed to drive the output tracking error to zero $\lim_{t \rightarrow \infty} y_c(t) - y(t) = 0$ in the presence of the bounded disturbance $f(x_1, x_2, t)$. It is possible to define the variable

$$\sigma = \dot{e} + ce, \quad c > 0 \quad (2.15)$$

where $e = y_c(t) - y(t)$ is the output tracking error. Now we have to design a conventional SMC u that drives $\sigma \rightarrow 0$ in finite time and keeps it at zero thereafter, bearing in mind that as soon as the sliding variable reaches zero the sliding mode starts and the output tracking error e in the sliding mode will obey the desired reduced (first)-order differential equation:

$$\sigma = \dot{e} + ce = 0 \quad (2.16)$$

that yields convergence to zero as time increases [9]. The sliding variable dynamics are derived as

$$\dot{\sigma} = \ddot{y}_c + \dot{y}_c - f(y, \dot{y}, t) - c\dot{y} - u \Rightarrow \dot{\sigma} = \varphi(y, \dot{y}, t) - u \quad (2.17)$$

The cumulative disturbance term $\varphi(y, \dot{y}, t)$ is assumed bounded, i.e. $\varphi(y, \dot{y}, t) \leq M$. Conventional SMC u can be designed [9] by using the sliding mode existence condition (2.10) rewritten in a form

$$\sigma \dot{\sigma} = -\bar{\alpha}|\alpha|, \quad \bar{\alpha} = \frac{\alpha}{\sqrt{2}} \quad (2.18)$$

Consequently

$$\sigma \dot{\sigma} = \sigma(\varphi(y, \dot{y}, t) - u) \leq |\sigma|M - \sigma u \quad (2.19)$$

and selecting

$$u = \rho \text{sign}(\sigma) \quad (2.20)$$

we obtain

$$\sigma \dot{\sigma} \leq |\sigma|(M - \rho) = -\bar{\alpha}\sigma \quad (2.21)$$

The control gain is computed as

$$\rho = M + \bar{\alpha} \quad (2.22)$$

The results of the simulation of system (2.14) with a conventional SMC control (2.16), (2.20), (2.22), the initial conditions $x_1(0) = 1, x_2(0) = 2$ the control gain $\rho = 6$, the parameter $c = 1.5$, the output reference profile $y_c = 2\cos(t)$, and the disturbance $f(x_1, x_2, t) = \sin(2t)$, are presented in Fig 2.10 [9].

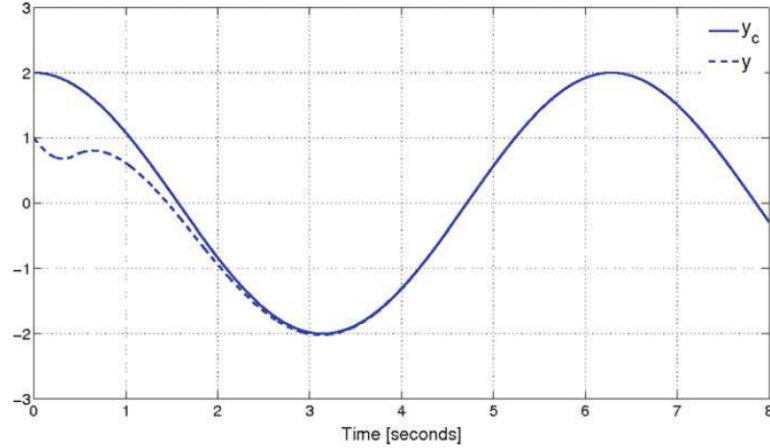


Figure 2.10: The reference profile tracking [9]

2.2.3 Super-Twisting SMC

For a variety of control issues with uncertainty, classic sliding modes offer robust and high-accuracy solutions. There are still two main restrictions, though. First, the constraint to be held at zero in conventional sliding modes must be of relative degree 1, meaning that the control needs explicitly appear in the first time derivative of the constraint. Hence, finding a suitable constraint is necessary. Second, if the control has any physical sense, high-frequency control switching may quickly result in intolerable practical issues (chattering effect). Consider a situation where the problem is to keep the sliding variable s at zero and the control only appears in \ddot{s} . Most frequently, $\sigma = s + \dot{s}$ is selected as the constraint function. $\dot{\sigma} = \dot{s} + \ddot{s}$, by design, contains the control and σ is able to be kept at zero in the classic sliding mode. As a result s tends asymptotically to zero, but it is impossible to exactly keep it at zero. To carry out this strategy, it is also necessary to compute \dot{s} . The second-order sliding mode method is capable of achieving both of these objectives: perfect robust differentiation and precisely maintaining $s = 0$. Assume that the goal is to maintain s at zero while the control is already present in \dot{s} . The use of standard sliding modes can readily solve this issue. Yet, the solution is frequently

undesirable due to the chattering effect. Considering the control derivative as a new virtual control is a possible solution. Therefore, using second-order sliding mode approach, the task can be precisely completed and in a finite amount of time by employing continuous. As a result, the chattering effect is greatly reduced.

In order to drive the sliding variable (2.15) to zero in finite time it is possible to select the following continuous control [9]:

$$u = c|\sigma|^{1/2}sign(\sigma), \quad c > 0 \quad (2.23)$$

Assuming $\varphi(y, \dot{y}, t) = 0$ in the sliding variable dynamics equation (2.17), the compensated sliding variable dynamics (2.17) becomes

$$\dot{\sigma} = -c|\sigma|^{1/2}sign(\sigma) \quad (2.24)$$

Integrating

$$|\sigma(t)|^{1/2} - |\sigma_0|^{1/2} = -\frac{c}{2}t \quad (2.25)$$

Therefore the time instant $t = t_r$ so that $\sigma(t_r) = 0$ is

$$t_r = \frac{c}{2}|\sigma_0|^{1/2} \quad (2.26)$$

So the control (2.23) drives the sliding variable to zero in finite time (2.26). However, in the case of $\varphi(y, \dot{y}, t) \neq 0$, the compensated-dynamics becomes

$$\dot{\sigma} = \varphi(y, \dot{y}, t) - c|\sigma|^{1/2}sign(\sigma) \quad (2.27)$$

and convergence to zero does not occur.

The disturbance would be entirely compensated for if the control function (2.23) could be modified, adding a term to make it begin tracking the disturbance $\varphi(y, \dot{y}, t) \neq 0$ in a finite amount of time. As soon as the disturbance is cancelled, the sliding variable dynamics will agree with Eq. (2.24), and $\sigma \rightarrow 0$ will also occur in a finite amount of time. Assuming $\varphi(y, \dot{y}, t) \leq C$ the following control

$$\begin{cases} u = c|\sigma|^{1/2}sign(\sigma) + w, \quad c = 1.5\sqrt{C} \\ \dot{w} = bsign(\sigma), \quad b = 1.1\sqrt{C} \end{cases} \quad (2.28)$$

makes the compensated-dynamics become

$$\begin{cases} \dot{\sigma} + c|\sigma|^{1/2}sign(\sigma) + w = \varphi(y, \dot{y}, t) \\ \dot{w} = bsign(\sigma) \end{cases} \quad (2.29)$$

The term w becomes equal to $\varphi(y, \dot{y}, t)$ in finite time, and therefore Eq. (2.29) becomes Eq. (2.24). Consequently $\sigma \rightarrow 0$ in finite time as well.

The control (2.28) is called super-twisting control, whose properties are:

- The super-twisting control (2.28) is a second-order sliding mode control, since it drives both $\sigma, \dot{\sigma} \rightarrow 0$ in finite time
- The super-twisting control (2.28) is continuous since both $c|\sigma|^{1/2}sign(\sigma)$ and the term $w = \int bsign(\sigma) dt$ are continuous. Now, the high-frequency switching term $sign(\sigma)$ is “hidden” under the integral [9].

The results of the simulation of the system (2.14) with the super-twisting control (2.15), (2.28), initial conditions $x_1(0) = 1, x_2(0) = -2$, the control gains $c = 13.5$ and $b = 88$, the parameter $C = 80$, the output reference profile $y_c = 2\cos(2t)$ and the disturbance $f(x_1, x_2, t) = \sin(2t)$, are presented in Figs. 2.11–2.14. The sliding variable is driven to zero in finite time (Fig. 2.11) by the continuous super-twisting control (Fig. 2.13). The high accuracy asymptotic output tracking (Fig. 2.12), which is achieved, is similar to that obtained with conventional SMC (Fig. 2.10), but is obtained by means of continuous control (Fig. 2.13) rather than high-frequency switching. Including the attenuated (by integration) high frequency switching term $sign(\sigma)$ (Fig. 2.14) in the super-twisting control (2.28) is mandatory because it compensates for the disturbance while retaining a continuity of the control function (Fig. 2.13) [9].

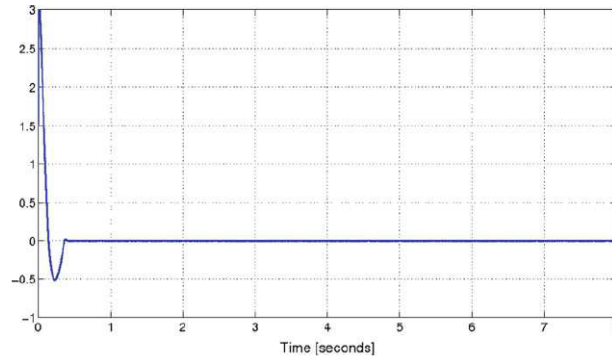


Figure 2.11: Sliding variable σ [9]

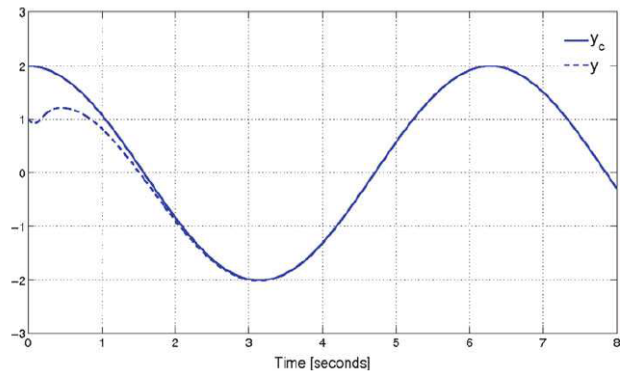


Figure 2.12: The reference profile tracking [9]

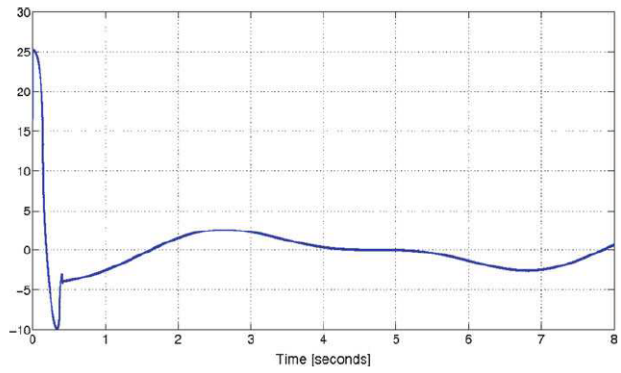


Figure 2.13: Super-twisting control [9]

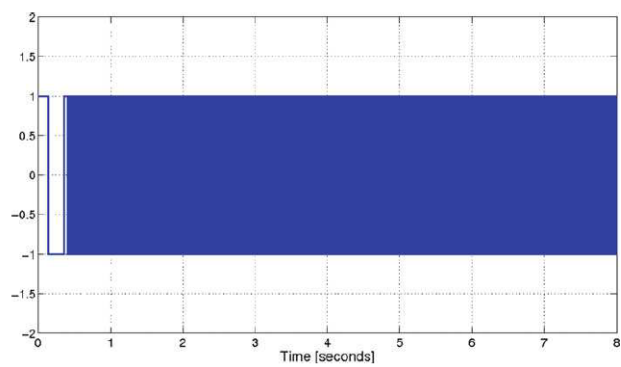


Figure 2.14: Time history of $\text{sign}(\sigma)$ [9]

Chapter 3

Solutions

3.1 Helix manoeuvre

As it was said in section 2.1, during the Observation Phase SROC performs 4 ellipses (with a radius of about 200 *m*) around Space Rider advancing along the *x* direction in the LVLH frame. Every ellipse is carried out in an orbital period of Space Rider:

$$\tau = 2\pi\sqrt{\frac{a^3}{\mu}} = 5553.63 \text{ s} \quad (3.1)$$

where *a* is the semi-major axis of Space Rider.

Therefore, the Helix manoeuvre can be seen as 2 coupled motions:

1. The motion around the *x* axis in the LVLH frame is like a uniform ellipsoidal motion with a constant angular velocity

$$\omega_x = \frac{2\pi}{\tau} = 0.001131 \text{ rad/s} \quad (3.2)$$

2. The motion along the *x* axis direction in the LVLH frame is like a uniform rectilinear motion with a constant velocity *v_x* so that SROC can travel 4 *km* along the *x* axis in four orbital periods of Space Rider.

So, the motion equations for the Helix manoeuvre are

$$\begin{cases} x = \int v_x dt \\ y = b_1 \cos(\omega_x t) \\ z = b_2 \sin(\omega_x t) \end{cases} \quad (3.3)$$

Where b_1 and b_2 are the semi-major and semi-minor axis of the ellipse that SROC performs around Space Rider every orbital period.

If $b_1 = 200 \text{ m}$, $b_2 = 150 \text{ m}$, $x_0 = -2000 \text{ m}$, $y_0 = -200 \text{ m}$ and $z_0 = 0 \text{ m}$, the Helix manoeuvre that SROC carries out in four orbital periods is depicted in Fig. 3.1.

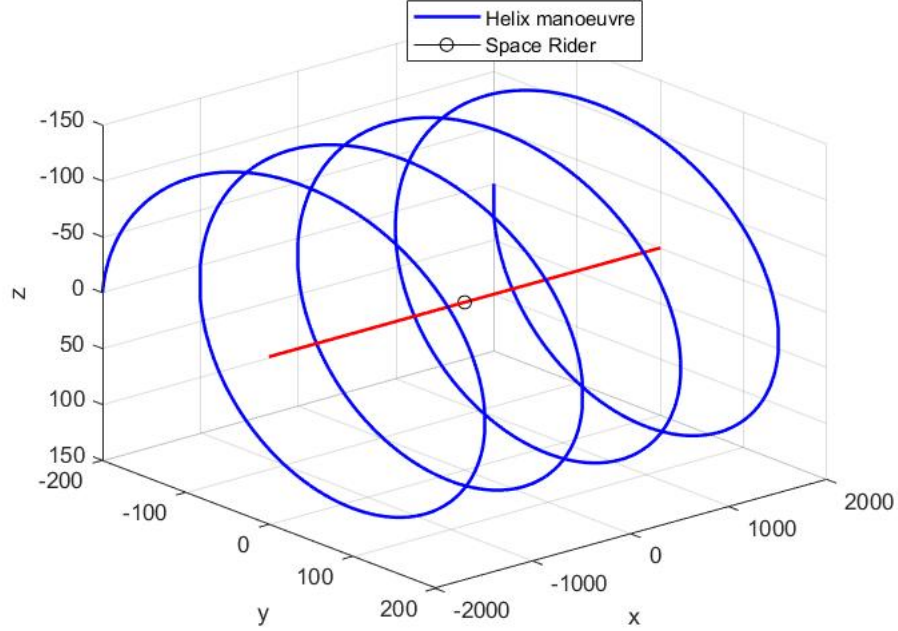


Figure 3.1: Helix manoeuvre (3.3) in four orbital periods

In order to consider a manoeuvre as similar as possible to the real case, it is possible to implement it using the Hill's equations:

$$\begin{cases} \ddot{x} = \frac{1}{m_c} F_x + 2\omega\dot{z} \\ \ddot{y} = \frac{1}{m_c} F_y - \omega^2 y \\ \ddot{z} = \frac{1}{m_c} F_z - 2\omega\dot{x} + 3\omega^2 z \end{cases} \quad (3.4)$$

where F_x , F_y and F_z are the forces provided by the thrusters and ω is the angular velocity of the target (Space Rider)

$$\omega = \sqrt{\frac{\mu}{a^3}} = 0.001131 \text{ rad/s} \quad (3.5)$$

These equations describe the relative position dynamics between the chaser (SROC) and the target (Space Rider) in the LVLH frame centered on the target. The Helix manoeuvre can be implemented through a Radial Boost in the $x-z$ plane and a sinusoidal motion for the y position (see the Appendix D for further details). For example, if the starting point's coordinates (in LVLH frame centered on Space Rider) of the Observation Phase are $x_0 = -2000\text{ m}$, $y_0 = 200\text{ m}$ and $z_0 = 20\text{ m}$ and the initial velocities are $\dot{x}_0 = 0\text{ m/s}$, $\dot{y}_0 = 0\text{ m/s}$ and $\dot{z}_0 = \Delta V_z = \frac{\omega}{4}\Delta x = 5.2360\text{ m/s}$ (as if the thrusters had provided an impulse along the z direction), the Helix manoeuvre that SROC carries out in four orbital periods is represented in Fig. 3.2.

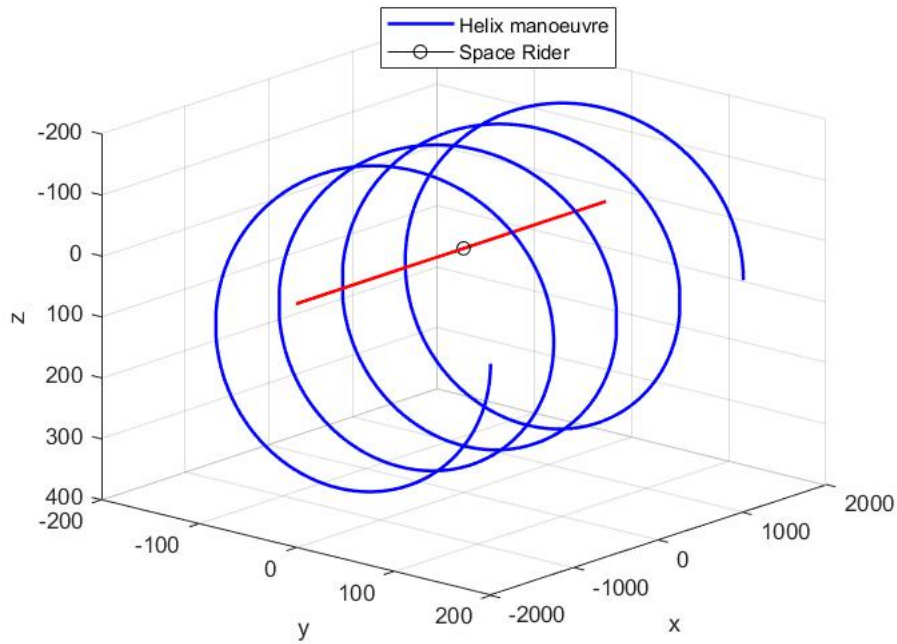


Figure 3.2: Helix manoeuvre (3.4) in four orbital periods

In this case the manoeuvre considered is more complex than the previous one because SROC does not always advance along the x direction, but, through every ellipse, it comes back (in this way the Observation Phase lasts again four orbital periods, but it is more accurate because SROC has a lower velocity along the x direction). Fig. 3.3 shows a focus of the manoeuvre represented in figure 3.2. It is also possible to change the initial conditions in order to ensure that the attitude control is always completed efficiently (see section 4).

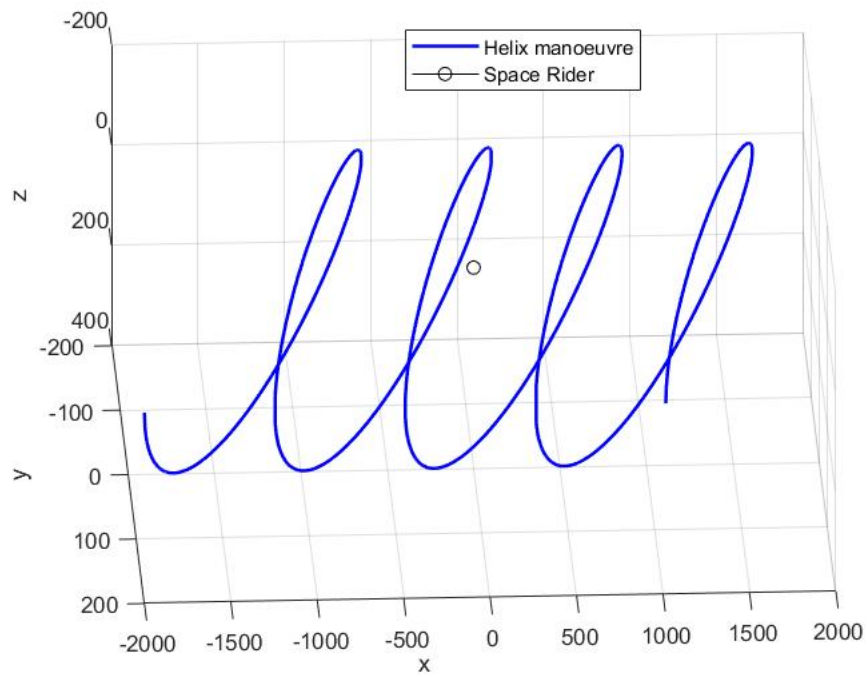


Figure 3.3: Focus of the Helix manoeuvre represented in Fig. 3.2

3.2 Attitude guidance

In order to generate the reference output for the attitude control tracking (Section 3.3), it is necessary to compute the reference attitude and the reference angular velocity.

For the reference attitude it is possible to use the Euler angles or the quaternions. In order to understand which way is more suitable for this case, it is possible to analyze a generic point of the Helix manoeuvre. In every point of the trajectory, SROC has to carry out a rotation around the y axis and the z axis (in the LVLH frame). For example, as it is possible to see in Fig. 3.4 and in Fig. 3.5, that represent the Helix manoeuvre (3.3) respectively in the $x - z$ plane and in the $x - y$ plane, SROC has to rotate about the y axis by a negative angle θ and about the z axis by a positive angle ψ to correctly point to Space Rider's center of mass. Therefore, as long as SROC has a negative x coordinate, the rotation angles around the y axis and z axis can be described by the following equations:

$$\theta = \operatorname{atan}\left(\frac{z}{|x|}\right) \quad (3.6)$$

$$\psi = -\operatorname{atan}\left(\frac{y}{|x|}\right) \quad (3.7)$$

While, as long as SROC has a positive x coordinate, the rotation angles around the y axis and z axis can be described by the following equations:

$$\theta = -\operatorname{atan}\left(\frac{z}{|x|}\right) + \pi \quad (3.8)$$

$$\psi = \operatorname{atan}\left(\frac{y}{|x|}\right) + \pi \quad (3.9)$$

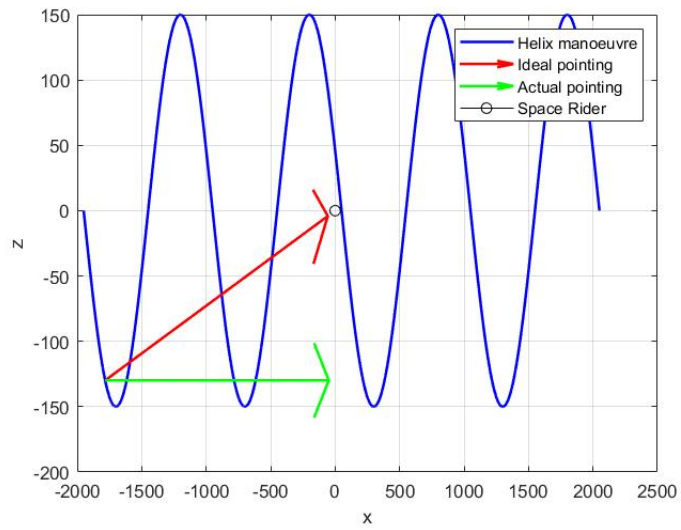


Figure 3.4: $x-z$ plane of the Helix manoeuvre (3.3) ($x_0 = -1950\text{ m}$, $y_0 = -200\text{ m}$ and $z_0 = 0\text{ m}$)

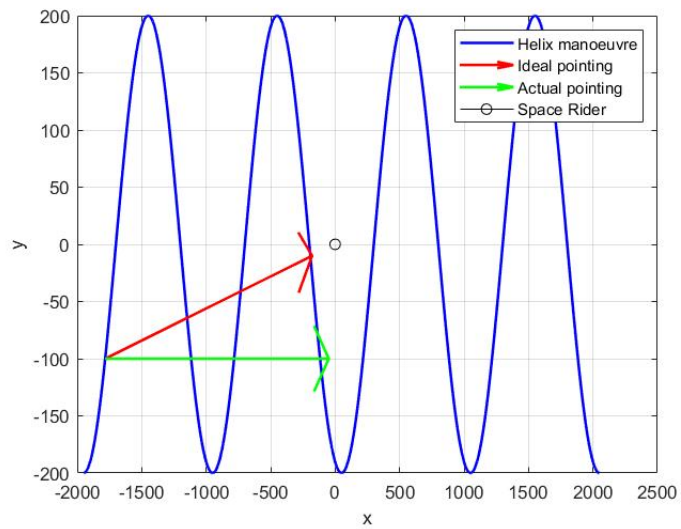


Figure 3.5: $x-y$ plane of the Helix manoeuvre (3.3) ($x_0 = -1950\text{ m}$, $y_0 = -200\text{ m}$ and $z_0 = 0\text{ m}$)

However, referring to Fig. 3.6 and Fig. 3.7, the equations that describe the rotation angles around the y axis and z axis become:

$$\begin{cases} \theta = \operatorname{atan}\left(\frac{z}{|x|}\right), & \text{if } x < 0 \\ \theta = -\operatorname{atan}\left(\frac{z}{|x|}\right) - \pi, & \text{if } x > 0 \end{cases} \quad (3.10)$$

$$\begin{cases} \psi = -\operatorname{atan}\left(\frac{y}{|x|}\right), & \text{if } x < 0 \\ \psi = \operatorname{atan}\left(\frac{y}{|x|}\right) + \pi, & \text{if } x > 0 \end{cases} \quad (3.11)$$

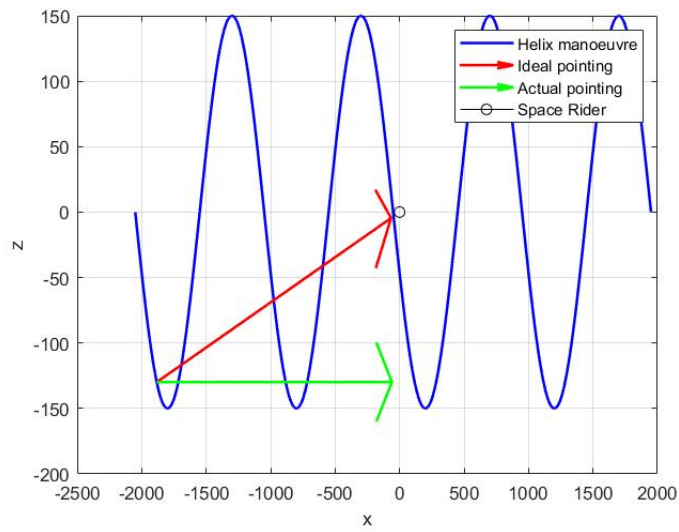


Figure 3.6: $x-z$ plane of the Helix manoeuvre (3.3) ($x_0 = -2050 \text{ m}$, $y_0 = -200 \text{ m}$ and $z_0 = 0 \text{ m}$)

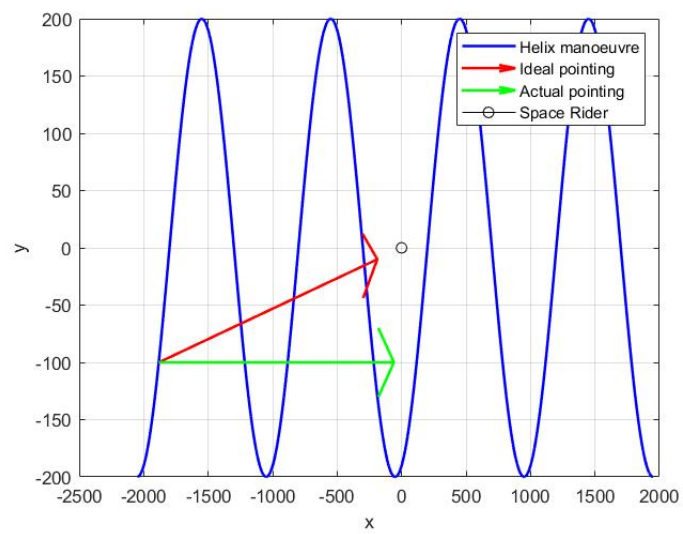


Figure 3.7: $x-y$ plane of the Helix manoeuvre (3.3) ($x_0 = -2050$ m, $y_0 = -200$ m and $z_0 = 0$ m)

In general, the new functions that describes the temporal evolution of θ and ψ depend on the last angle in the transition from before to after Space Rider's center of mass. Therefore, if the reference generator computes the wrong angle of rotation, the controller may not be able to follow the desired attitude because of a discontinuity in the attitude angles functions. Moreover, the angles computed through the equations (3.6)-(3.9) or (3.10)-(3.11) are the angles between the ideal vector pointing and the actual vector pointing, so they are not actually the Euler Angles in a classical rotation sequence 3 – 1 – 3 (Appendix B). Since the objective is to implement a robust algorithm that computes the reference attitude according to every type of manoeuvre (even if the impulse provided by the thrusters is not fully executed), it is necessary to change the method to compute the reference attitude.

Therefore, in this case, in order to compute the correct reference attitude it is necessary to use the Euler's Theorem: "The most general motion of a rigid body with one point fixed is a rotation about an axis through that point". In fact, in each point of the trajectory it is possible to compute the Euler's axis $\vec{a} = [a_1 \ a_2 \ a_3]^T$ (that is orthogonal to both the ideal or reference vector pointing and the actual one) and, consequentially, the only rotation angle α about this axis (Appendix C). In this way, the the Euler's axis \vec{a} and rotation angle α about this axis are:

$$\vec{a} = \frac{\vec{r}_{actual} \wedge \vec{r}_{ideal}}{\|\vec{r}_{actual} \wedge \vec{r}_{ideal}\|} \quad (3.12)$$

$$\alpha = \text{acos}\left(\frac{\vec{r}_{actual} \cdot \vec{r}_{ideal}}{\|\vec{r}_{actual}\| \|\vec{r}_{ideal}\|}\right) \quad (3.13)$$

Where \vec{r}_{actual} is the real vector pointing and \vec{r}_{ideal} is the ideal vector pointing. In Fig. 3.8 the Eules's axis in a generic point of the trajectory is represented.

It is now possible to compute the reference quaternion $\vec{q}_r = [q_{r_0} \ q_{r_1} \ q_{r_2} \ q_{r_3}]^T$:

$$\begin{cases} q_{r_0} = \cos\left(\frac{\alpha}{2}\right) \\ q_{r_1} = a_1 \sin\left(\frac{\alpha}{2}\right) \\ q_{r_2} = a_2 \sin\left(\frac{\alpha}{2}\right) \\ q_{r_3} = a_3 \sin\left(\frac{\alpha}{2}\right) \end{cases} \quad (3.14)$$

Since the control torque (see section 3.3) also needs the reference angular velocity $\vec{\omega}_r = [\omega_{r_x} \ \omega_{r_y} \ \omega_{r_z}]^T$ and its temporal derivative $\dot{\vec{\omega}}_r$, (3.15) shows the relation between the first one and the temporal derivative of the reference quaternion $\dot{\vec{q}}_r$:

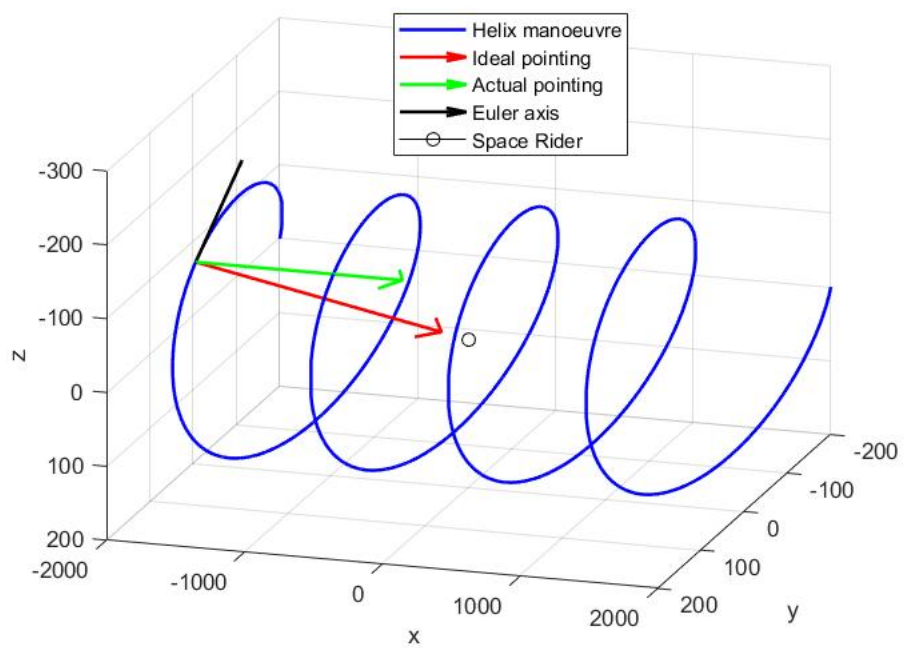


Figure 3.8: Eules's axis in a generic point of the trajectory

$$\begin{Bmatrix} \dot{\vec{q}}_{r_v} \\ \dot{q}_{r_0} \end{Bmatrix} = \frac{1}{2} \begin{bmatrix} -q_{r_v}^x + q_{r_0} I \\ \vec{q}_{r_v} \end{bmatrix} \begin{Bmatrix} \vec{\omega}_r \\ 0 \end{Bmatrix} \quad (3.15)$$

where I is the identity matrix, $\vec{q}_{r_v} = [q_{r_1} \ q_{r_2} \ q_{r_3}]^T$ and q_{r_0} are, respectively, the vectorial part and the scalar part of the reference quaternion and $q_{r_v}^x$ is defined as

$$q_{r_v}^x = \begin{bmatrix} 0 & -q_{r_3} & q_{r_2} \\ q_{r_3} & 0 & -q_{r_1} \\ -q_{r_2} & q_{r_1} & 0 \end{bmatrix} \quad (3.16)$$

and, consequently,

$$\vec{\omega}_r = \left(\frac{1}{2} [q_{r_v}^x + q_{r_0} I] \right)^{-1} \dot{\vec{q}}_{r_v} \quad (3.17)$$

$$\dot{\vec{\omega}}_r = \frac{d\vec{\omega}_r}{dt} \quad (3.18)$$

3.3 Attitude control with Super-Twisting SMC

Considering what it has been said in section 1 and in section 2.2.3, a robust Sliding Mode Control is needed to carry out the attitude tracking control during the Helix manoeuvre; in fact, in this section a robust Super-Twisting SMC is proposed.

Considering SROC as a rigid body with inertia matrix J , it is possible to define the following variables:

- $\vec{\omega} = [\omega_x \ \omega_y \ \omega_z]^T$ angular velocity in body frame
- $\vec{q} = [q_0 \ q_1 \ q_2 \ q_3]^T$ quaternions
- $\vec{u} = [u_x \ u_y \ u_z]^T$ external moment in body frame.

The state equations are given by the quaternion kinematic equation and the Euler dynamic equation:

$$\dot{\vec{q}} = \frac{1}{2} Q \vec{\omega} \quad (3.19)$$

$$\dot{\vec{\omega}} = J^{-1} \vec{u} - J^{-1} (\vec{\omega} \wedge (J \vec{\omega})) \quad (3.20)$$

where

$$Q = \begin{bmatrix} -q_1 & -q_2 & -q_3 \\ q_0 & -q_3 & q_2 \\ q_3 & q_0 & -q_1 \\ -q_2 & q_1 & q_0 \end{bmatrix} \quad (3.21)$$

The goal of control law is to make the state vector $(\vec{q}, \vec{\omega})$ track the time-varying reference vector $(\vec{q}_r, \vec{\omega}_r)$. It is thus important to measure the distance between the reference and the actual state. To this aim, we define:

- the angular velocity tracking error

$$\vec{\omega}_{err} = \vec{\omega}_r - \vec{\omega}$$

- the quaternion tracking error

$$\vec{q}_{err} = [q_{err_0} \ \vec{q}_{err_v}]^T = \vec{q}^* \otimes \vec{q}_r$$

where \otimes is the quaternion multiplication (see Appendix C).

Following the procedure of [34], the sliding surface, according to (2.16), is:

$$\vec{s} = \vec{\omega}_{err} + k_2 \vec{q}_{err}, \quad k_2 > 0 \quad (3.22)$$

On the sliding surface, the tracking error converges to 0. The derivative of the sliding surface is:

$$\begin{aligned} \dot{\vec{s}} &= \dot{\vec{\omega}}_r - \dot{\vec{\omega}} + k_2 \dot{\vec{q}}_{err} = \\ &= \dot{\vec{\omega}}_r + J^{-1} \vec{\omega} \wedge (J \vec{\omega}) - J^{-1} \vec{u} + \frac{k_2}{2} \left(q_{err_0} \vec{\omega}_{err} + \vec{q}_{err_v} \wedge (\vec{\omega}_r + \vec{\omega}) \right) \end{aligned}$$

Imposing $\dot{\vec{s}} = 0$ to make the sliding surface invariant and inverting wrt \vec{u} the above expression,

$$\vec{u}_s = J \left(\dot{\vec{\omega}}_r + \frac{k_2}{2} (q_{err_0} \vec{\omega}_{err} + \vec{q}_{err_v} \wedge (\vec{\omega}_r + \vec{\omega})) \right) + \vec{\omega} \wedge (J \vec{\omega}) \quad (3.23)$$

Finally, according to (2.28), a further term is added to make the sliding surface attractive. The complete control law is:

$$\begin{cases} \vec{u} = \vec{u}_s + k_1 |\sigma|^{1/2} \text{sign}(\sigma) + w, \quad k_1 > 0 \\ \dot{w} = \alpha \text{sign}(\sigma), \quad \alpha > 0 \end{cases} \quad (3.24)$$

Therefore, the tracking attitude control during the Helix manoeuvre is carried out through the Super-Twisting SMC control law (3.24).

Chapter 4

Mathematical model and simulations

4.1 Mathematical model

This section explains the procedures through which the CubeSat and the disturbances torques have been modeled in order to implement an orbital simulator. In this way it is possible to simulate the Helix manoeuvre and verify that the attitude tracking control is effectively carried out.

The sensors for position and attitude measurement, the GNC functions, which are implemented in software in the onboard computer, i.e. the navigation, guidance, and control functions, and the thrusters and other actuators for attitude and position control are all included in the control loops for attitude and trajectory control. Fig. 4.1 is a block diagram of a typical control loop for one of the six degrees of freedom (DOF). Since the focus of the thesis is Guidance and Control, in section 4.2 all the blocks concerning sensors and navigation filter will be neglected.

4.1.1 SROC attitude dynamics and kinematics

Since SROC is modeled on a rigid body with its inertia matrix J , its attitude dynamics can be described by the Euler's equation:

$$\dot{\vec{\omega}} = J^{-1}(\vec{M} - \vec{\omega} \wedge (J\vec{\omega})) \quad (4.1)$$

with

$$\vec{M} = \vec{M}_{ext} + \vec{M}_c \quad (4.2)$$

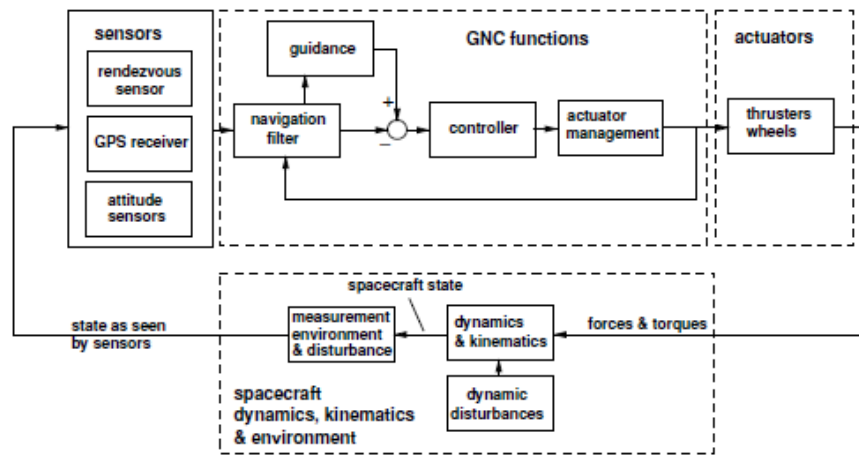


Figure 4.1: GNC functions [35]

and

$$\vec{M}_c = -\vec{M}_{RW} \quad (4.3)$$

where \vec{M}_{ext} is the total disturbance torque (see section 4.1.3) due to the space environment in which Space Rider and SROC operate, \vec{M}_c is the control torque \vec{u} (3.24) computed by the controller block (in this case by the Super-Twisting SMC algorithm) and \vec{M}_{RW} is the torque provided by the 4 Reaction Wheels. Since the actuators that provide the control torque are Reaction Wheels that are considered as momentum exchange devices, by accelerating a wheel in one direction about the wheel spin-axis, the wheel applies a reaction torque to the platform in the opposite direction (in order to maintain the total angular momentum constant, in absence of external torques acting on the spacecraft, if the angular momentum of the wheel is changed, there must be a corresponding opposite change in angular momentum of the platform). Therefore, Eq. (4.1) becomes:

$$\dot{\vec{\omega}} = J^{-1}(\vec{M}_{ext} - \vec{M}_{RW} - \vec{\omega} \wedge (J\vec{\omega} + h_{RW})) \quad (4.4)$$

where

$$\vec{h}_{RW} = J_{RW} \vec{\omega}_{RW} \quad (4.5)$$

$$\vec{M}_{RW} = \dot{\vec{h}}_{RW} = J_{RW} \dot{\vec{\omega}}_{RW} \quad (4.6)$$

\vec{h}_{RW} is the angular momentum, J_{RW} is the inertia matrix and $\vec{\omega}_{RW}$ is the angular velocity of the Reaction Wheels.

For the attitude kinematics, on the other hand, equation (3.19) is used.

4.1.2 Reaction Wheels model

Since the 4 Reaction Wheels of SROC are disposed in a pyramidal configuration (Fig 4.2), in order to transform the control torque from body axis to 4 RWs directions it is useful to evaluate the rotation matrix Z :

$$Z = \begin{bmatrix} \cos(\beta)\cos(\alpha) & -\cos(\beta)\sin(\alpha) & -\cos(\beta)\cos(\alpha) & \cos(\beta)\sin(\alpha) \\ \cos(\beta)\sin(\alpha) & \cos(\beta)\cos(\alpha) & -\cos(\beta)\sin(\alpha) & -\cos(\beta)\cos(\alpha) \\ \sin(\beta) & \sin(\beta) & \sin(\beta) & \sin(\beta) \end{bmatrix} \quad (4.7)$$

so

$$\vec{M}_{4RW} = Z^{-1} \vec{M}_c \quad (4.8)$$

In this way, according to (4.5) and (4.6), it is possible to compute $\dot{\vec{\omega}}_{RW}$, $\vec{\omega}_{RW}$ (that has a lower limit and an upper one due to mechanical limitation) and \vec{h}_{RW} . Finally, it is necessary to transform the torque \vec{M}_{4RW} provided by the 4 Reaction Wheels into body axis:

$$\vec{M}_{RW} = Z \vec{M}_{4RW} \quad (4.9)$$

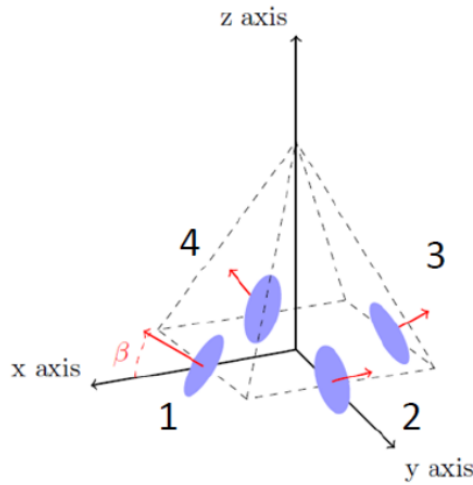


Figure 4.2: 4 Reaction Wheels in a pyramidal configuration [33]

A low pass filter followed by a saturation block, that provides the maximum applicable torque (due to electrical limitation) is used to model the Reaction Wheels' dynamics.

4.1.3 External disturbances

In the low Earth orbit (LEO) environment, where Space Rider and SROC operate, the four primary sources of orbital disturbance that have an impact on a spacecraft attitude and orbit dynamics are: residual atmospheric drag, gravitational disturbances, solar radiation, and electromagnetic disturbances. The last two sources show a smaller magnitude in comparison to other ones, hence they will be neglected.

Atmospheric drag

The leftover atmospheric gases that strike the spacecraft's surface are what cause the drag disturbance. At high altitude, greater than 100 km., the residual atmosphere can no longer be viewed as a continuum media and must instead be modeled as a discrete medium using the free molecular flow model. In fact, the momentum transfer between the spacecraft and the gas particles is taken into account while computing the residual atmospheric drag. Depending on a number of variables, including surface and incident flow temperature, the molecular weight of the particles, the spacecraft's speed, and others, some particles may be entirely or partially reflected when striking the spacecraft's surface. The accommodation coefficient has been established to take these influences into account when computing Cook's spacecraft drag coefficient [36]. Cook's analysis demonstrates that, in some circumstances, it may be beneficial to calculate a spacecraft's drag coefficient precisely. However, because atmospheric models include other uncertainties (such as the determination of the precise temperature, density, magnetic flux, and others), the computation of the total drag force is impacted by uncertainties that are greater than those that affect the drag coefficient [32].

For the purpose of this work, the computation of the residual drag force is carried out using the following method:

$$F_D = \frac{1}{2}\rho V^2 S_{front} C_D \quad (4.10)$$

Where F_D is the total drag force acting on the center of pressure of the spacecraft and aligned with the spacecraft velocity V , ρ is the atmospheric density, S_{front} is the exposed frontal area perpendicular to the direction of motion and C_D is the drag coefficient. Cook's study indicates that the C_D value is set at 2.2. The value of C_D may be increased up to 10 – 20 %, taking the worst-case scenario into account, in order to account for uncertainties in both the drag coefficient computation and the center of pressure assessment.

Therefore, the drag torque is:

$$\vec{M}_D = \vec{r}_{cp} \wedge \vec{F}_D \quad (4.11)$$

where \vec{r}_{cp} is the distance between the center of pressure and the center of mass of the spacecraft.

Gravity gradient

Gravitational torque is due to the differential gravitational force which acts on the spacecraft. As shown in Fi. 4.3, two equal masses m orbiting the Earth linked together by a mass-less rigid beam of length l are subjected to two different forces:

$$F_1 = m \frac{\mu}{R_1^2} \quad F_2 = m \frac{\mu}{R_2^2}$$

where R_1 and R_2 are the distances from the center of the Earth of the two masses, respectively. Since $R_1 < R_2$, it follows that $F_1 > F_2$; hence a torque M_{gg} is generated [32]

$$M_{gg} = (F_2 - F_1) \frac{l}{2} \sin(\alpha)$$

When this behavior is applied to the entire body of a spacecraft, the following outcome is achieved:

$$\vec{M}_{gg} = \frac{3\mu}{r^5} \vec{r}_B \wedge (J\vec{r}_B) \quad (4.12)$$

where r is the norm of the position vector from of the Earth and \vec{r}_B is the position vector in body axis, that is obtained trough the rotation matrix $[L_{BI}]$ (see Appendix C)

$$\vec{r}_B = [L_{BI}] \begin{bmatrix} 0 \\ 0 \\ -r \end{bmatrix} \quad (4.13)$$

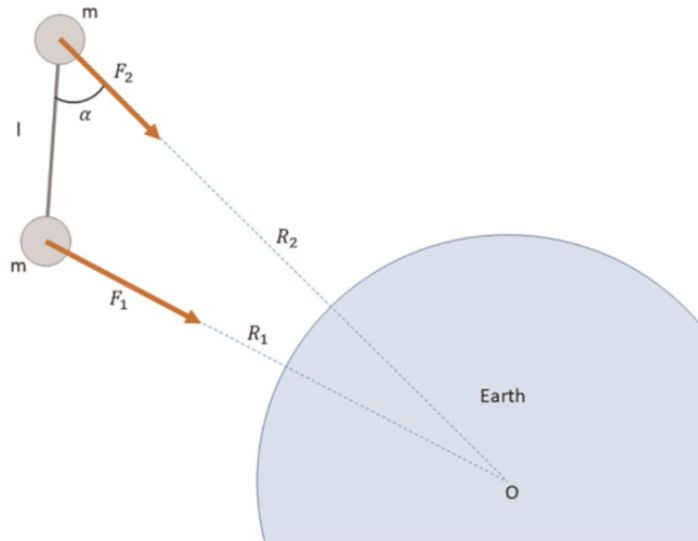


Figure 4.3: Simple gravity gradient torque example [32]

Solar radiation pressure

Photons from the Sun's rays that interact with the surface of the spacecraft to exchange momentum create this torque. Clearly, this disturbance is only evident when the spacecraft's orbit is in the direction of the sun. This disturbance does not exist when the Earth's shadow covers the spacecraft's orbit. The strength of this torque is influenced by the Sun's activity, which varies throughout the year in accordance with its cycles. The magnitude of this torque is typically smaller than the impact of drag and gravity on spacecraft with a compact design and without lengthy appendages; hence, this disturbance may be disregarded. The solar radiation torque is:

$$\vec{M}_{sp} = \vec{r}_s \wedge (\vec{F}_{sp}) \quad (4.14)$$

where

$$F_{sp} = (1 + k)p_s S \quad (4.15)$$

is the solar radiation force, k is the reflectivity (from 0 to 1), $p_s = 4.5 \cdot 10^{-6} N/m^2$ is the solar pressure near the Earth and \vec{r}_s is the vector from the center of mass of the spacecraft to optical its center of pressure.

Electromagnetic disturbances

This torque is due to the interaction between the residual magnetic dipole \vec{d} and the magnetic field \vec{B} generated by the Earth such that

$$\vec{M}_{mag} = \vec{d} \wedge (\vec{B}) \quad (4.16)$$

Typically, a spacecraft's residual magnetic dipole is minimized or neutralized during design. However, the employment of magnetic torquers produces a desirable magnetic dipole in order to obtain a particular torque, which can then be used to desaturate momentum actuators (reaction wheels and gyroscopes) or control the attitude of very small spacecraft (often CubeSats). In general, this disruption can be disregarded because the spacecraft's designer was able to appropriately account for the magnetic dipole.

4.2 Simulations

A small satellite orbital simulator has been developed in a MATLAB/Simulink environment to evaluate the tracking attitude control performance under disturbances,

according to the mathematical model of section 4.1. The diagram in Fig. 4.4 represents its structure and data flow, including attitude dynamics and kinematics, environmental disturbance model, control block and reference generator (guidance block).

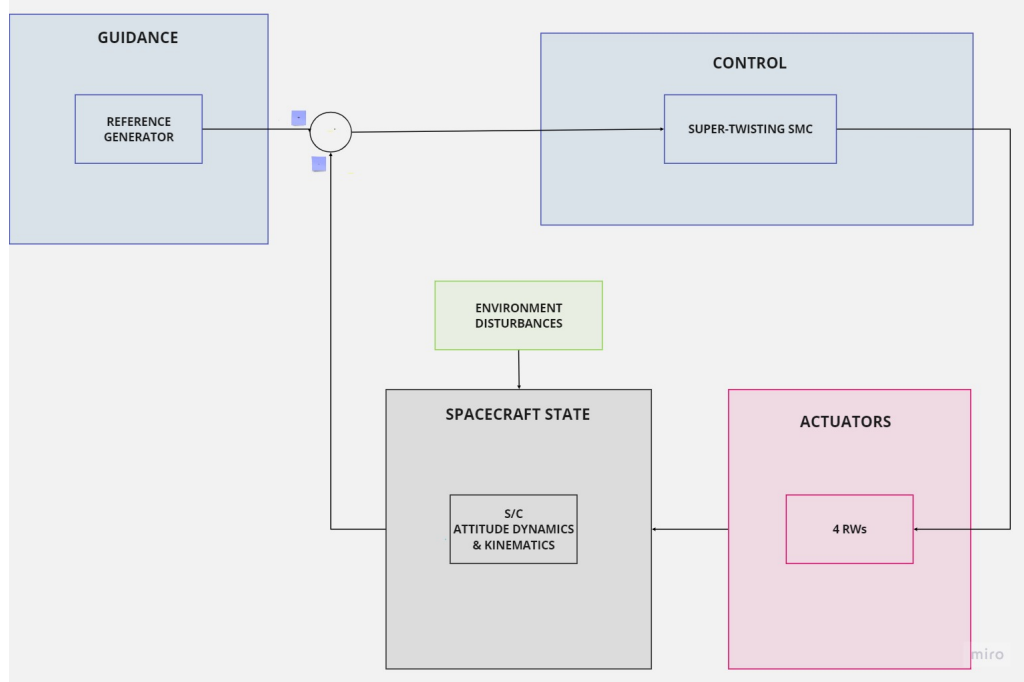


Figure 4.4: Orbital simulator architecture

In order to ensure that SROC is correctly pointing the center of mass of Space Rider, it is possible to rotate the versor $[1 \ 0 \ 0]^T$ (in LVLH frame), that represents the axis perpendicular to the face where the camera is collocated (hence the real pointing vector), according to the rotation matrix L_{BI} (see Appendix C) computed from the quaternions during the simulation. In this way the effective pointing vector carried out during the Helix manoeuvre is:

$$\vec{r}_{pointing} = [L_{BI}]^T \begin{bmatrix} 1 \\ 0 \\ 0 \end{bmatrix} \quad (4.17)$$

where

$$[L_{BI}] = (q_0^2 - \vec{q}_v \cdot \vec{q}_v)I + 2\vec{q}_v \vec{q}_v^T - 2q_0Q \quad (4.18)$$

4.2.1 Nominal scenario

These simulations are carried out for both the manoeuvres (3.3) and (3.4) described in section 3.1. The control gains of the Eq. (3.22) and (3.24), identified through the try and error process based on simulation sessions, have the values reported in Table 4.1 and in Table 4.2, respectively for the Helix manoeuvre (3.3) and (3.4).

Parameter	Value
α	0.01
k_1	6
k_2	6

Table 4.1: Control gains for the simulations of the Helix manoeuvre (3.3)

Parameter	Value
α	10^{-50}
k_1	0.08
k_2	6

Table 4.2: Control gains for the simulations of the Helix manoeuvre (3.4)

4.2.2 Robustness analysis

A Monte Carlo simulation campaign consists of a set of simulation runs each using different values of the parameters defining the statistical ensemble. Monte Carlo simulation campaigns should be used:

- If the requirement is imposed only for a specified fraction of the statistical ensemble
- If the parameter space involved is sufficiently large and complex that it is not possible to use analysis to determine a single worst case scenario to be simulated.

An appropriate verification of the compliance with the requirement cannot be performed if a sufficiently large number of simulation runs are not used. For

a requirement specified with confidence level P_c , the minimum number of runs required to verify that the requirement holds (to a verification confidence level of 95 %), is given in Table 4.3. This table makes assumptions about how many actual cases of requirement violation (pointing error $>$ tolerance) are seen [37]. According to [38], it is possible to define:

- Absolute Performance Error (APE), the difference between the target (commanded) parameter (attitude, geolocation, etc.) and the actual parameter in a specified reference frame, hence, in this case

$$APE = \text{acos}\left(\frac{\vec{r}_{pointing} \cdot \vec{r}_{ideal}}{\|\vec{r}_{pointing}\| \|\vec{r}_{ideal}\|}\right) \quad (4.19)$$

- Mean Performance Error (MPE), the mean value of APE over a specified time interval Δt
- Relative Performance Error (RPE), the difference between the APE at a given time within a time interval, Δt , and the MPE over the same time interval.

$$RPE = APE - MPE$$

where $\vec{r}_{pointing}$ the effective pointing vector (4.17) carried out during the Helix manoeuvre and \vec{r}_{ideal} is the ideal one. Therefore, the fail numbers of Table 4.3 refer to an Absolute Performance Error (APE) bigger than a pre-established tolerance.

Requirement confidence level P_c	$N_{fail} = 0$	$N_{fail} = 1$	$N_{fail} = 2$	$N_{fail} = 3$
68 %	7	12	17	21
95 %	58	92	123	152
99.73 %	1108	1755	2329	2869

Table 4.3: Minimum number of simulation runs required to verify a requirement at confidence level P_c [37]

In this paragraph, the robustness of the Super-Twisting SMC is verified through the results of 58 Monte Carlo simulations. Each simulation randomly varies for the initial conditions inside the range reported in Table 4.4.

Parameter	Value	Uncertainties
SROC mass m	20 kg	$\pm 20\%$
Initial attitude angle ϕ	0°	$\pm 10^\circ$
Initial attitude angle θ	0°	$\pm 10^\circ$
Initial attitude angle ψ	0°	$\pm 10^\circ$
Initial angular velocity ω_x	0 rad/s	± 0.02 rad/s
Initial angular velocity ω_y	0 rad/s	± 0.02 rad/s
Initial angular velocity ω_z	0 rad/s	± 0.02 rad/s

Table 4.4: Initial conditions of the simulation with the boundaries of uncertainties

4.2.3 Off-nominal scenario

Finally, a robustness analysis also for the off nominal scenario, due to a casual failure of one of the four Reaction Wheels, has been conducted. Each simulation randomly varies for the initial conditions inside the range reported in Table 4.4.

Chapter 5

Results and discussions

5.1 Nominal scenario

In this section all the results of the simulations, presented in sections 4.2.1 - 4.2.3, are shown.

5.1.1 Helix manoeuvre (3.3)

Case 1

The Helix manoeuvre (3.3) carried out in four orbital periods (3.1) of Space Rider, with the initial conditions reported in Table 5.1,

Parameter	Value	Measure of unit
b_1	200	m
b_2	150	m
x_0	-2000	m
y_0	-200	m
z_0	0	m
\vec{q}	$[1 \ 0 \ 0 \ 0]^T$	-
$\vec{\omega}$	$[0 \ 0 \ 0]^T$	rad/s

Table 5.1: Initial conditions of the simulation

is depicted in Fig. 5.1.

Fig. 5.2 - 5.7 represent the temporal evolution of the quaternions, the quaternion error, that describes the pointing error, and also of the angular velocity error. Fig. 5.8, instead, shows a zoom of Fig. 5.5.

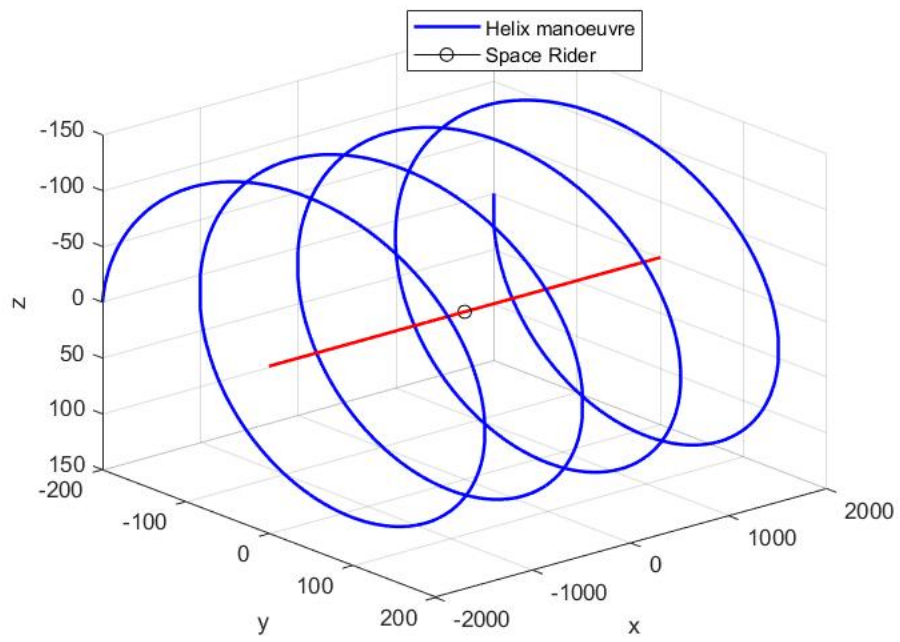


Figure 5.1: Helix manoeuvre (3.3) in four orbital periods (Table 5.1)

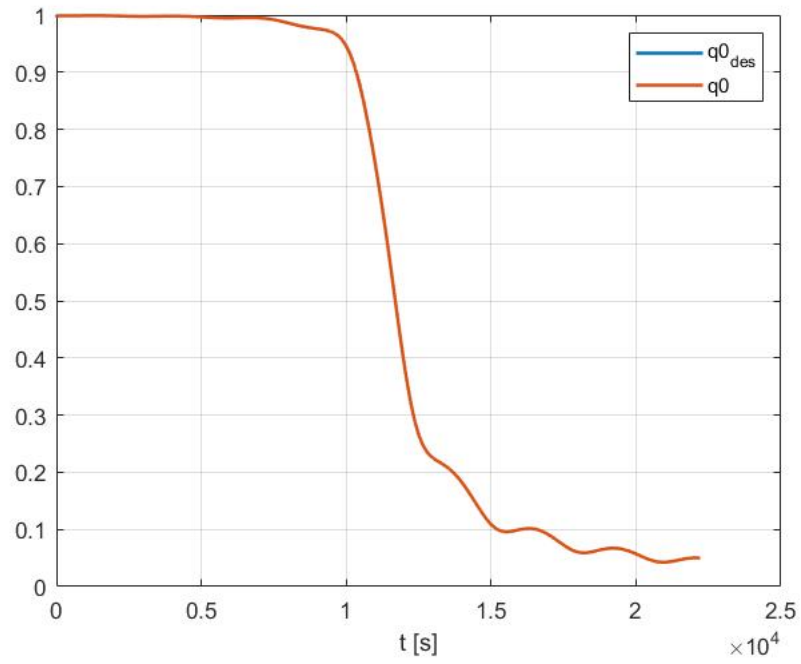


Figure 5.2: Temporal evolution of q_0 during tracking attitude control (Table 5.1)

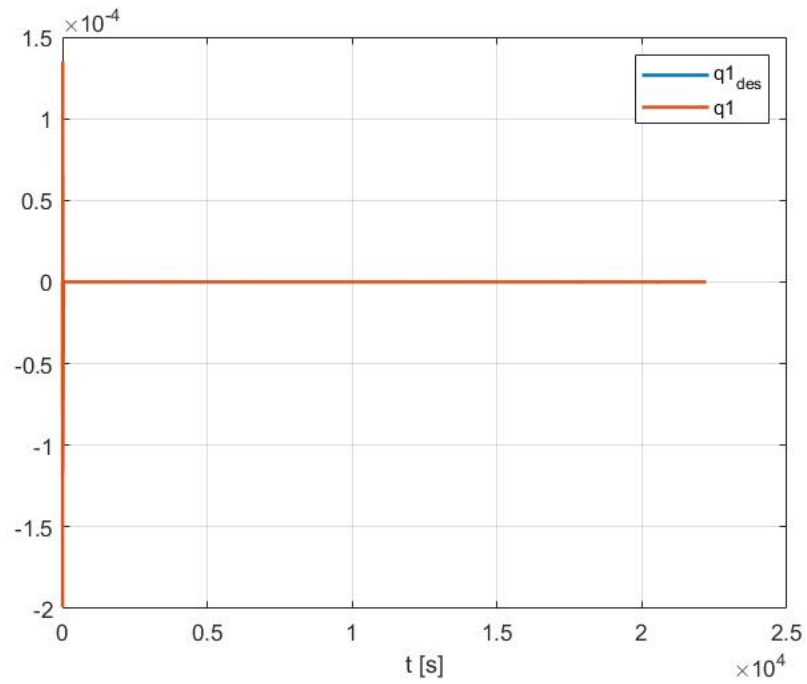


Figure 5.3: Temporal evolution of q_1 during tracking attitude control (Table 5.1)

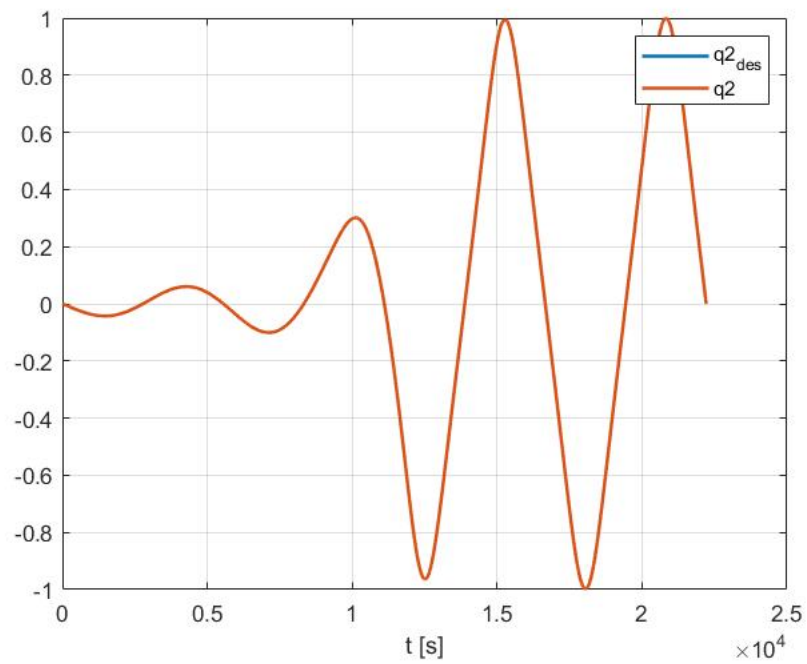


Figure 5.4: Temporal evolution of q_2 during tracking attitude control (Table 5.1)

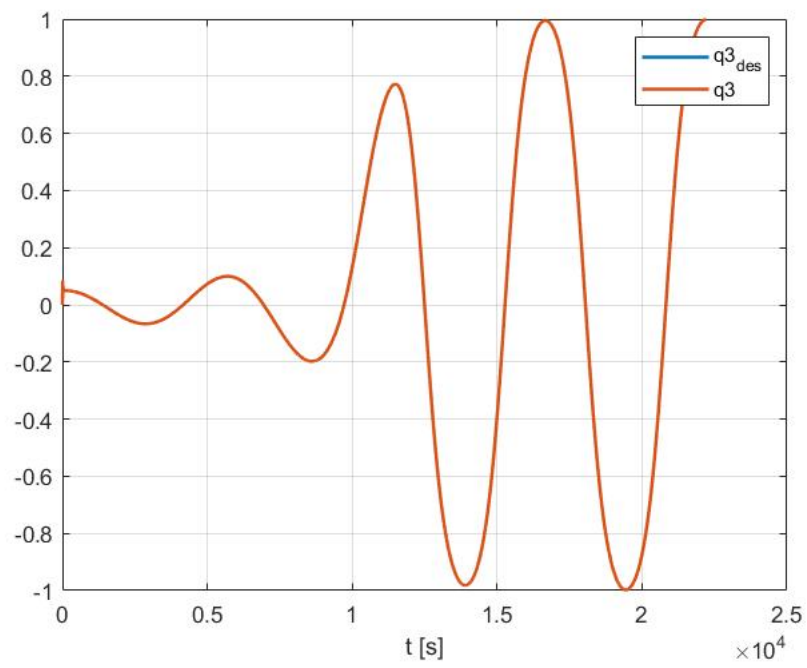


Figure 5.5: Temporal evolution of q_3 during tracking attitude control (Table 5.1)

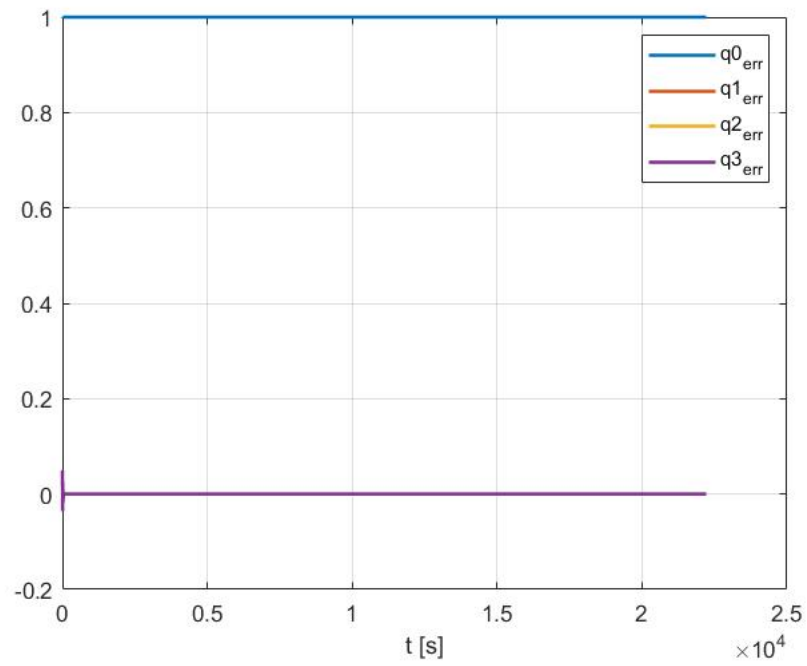


Figure 5.6: Temporal evolution of the quaternion error during tracking attitude control (Table 5.1)

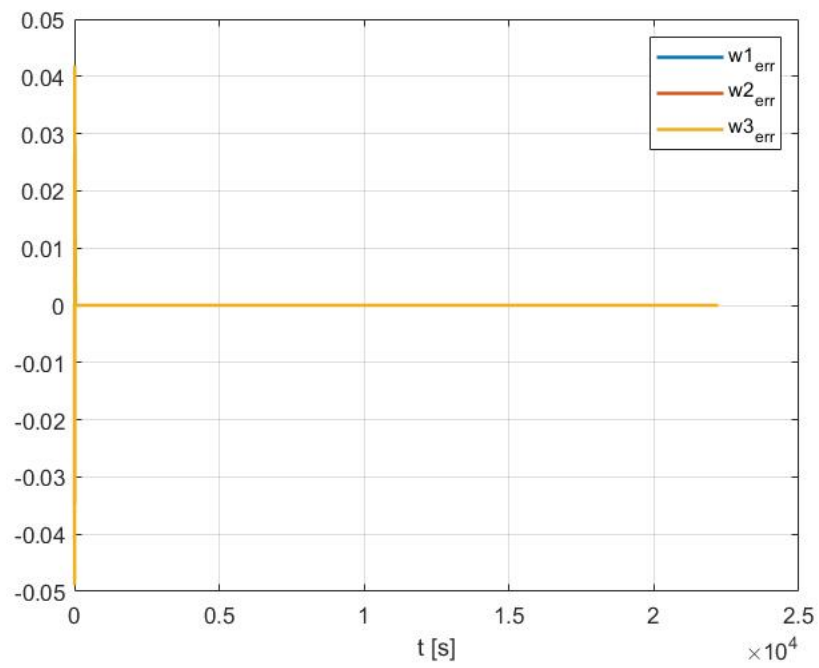


Figure 5.7: Temporal evolution of the angular velocity error during tracking attitude control (Table 5.1)

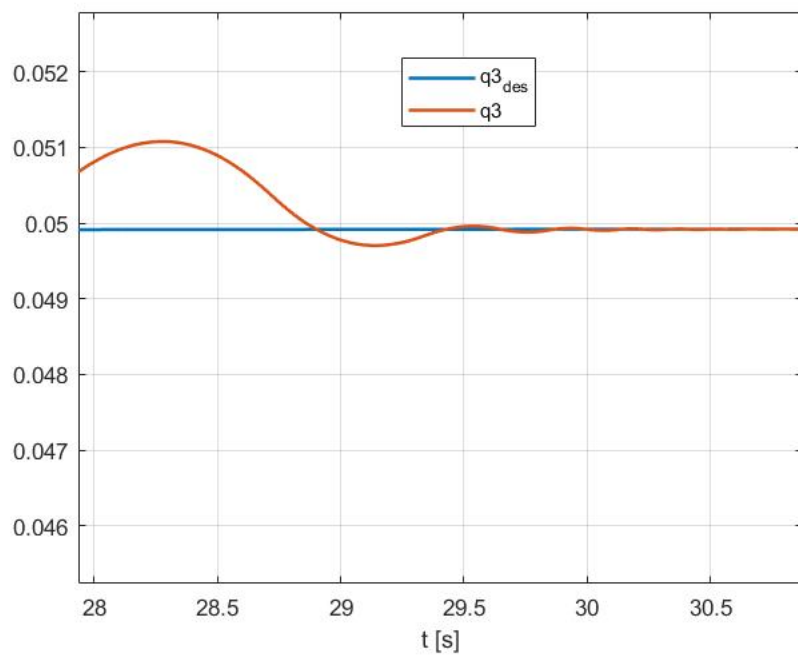


Figure 5.8: Zoom of Fig. 5.5

Case 2

If the initial conditions are those reported in Table 5.2,

Parameter	Value	Measure of unit
b_1	200	m
b_2	150	m
x_0	-2000	m
y_0	200	m
z_0	0	m
\vec{q}	$[1 \ 0 \ 0 \ 0]^T$	-
$\vec{\omega}$	$[0 \ 0 \ 0]^T$	rad/s

Table 5.2: Initial conditions of the simulation

the Helix manoeuvre (3.3) carried out in four orbital periods (3.1) of Space Rider is depicted in Fig. 5.9, while Fig. 5.10 - 5.15 represent the temporal evolution of the quaternions, quaternion error and angular velocity error.

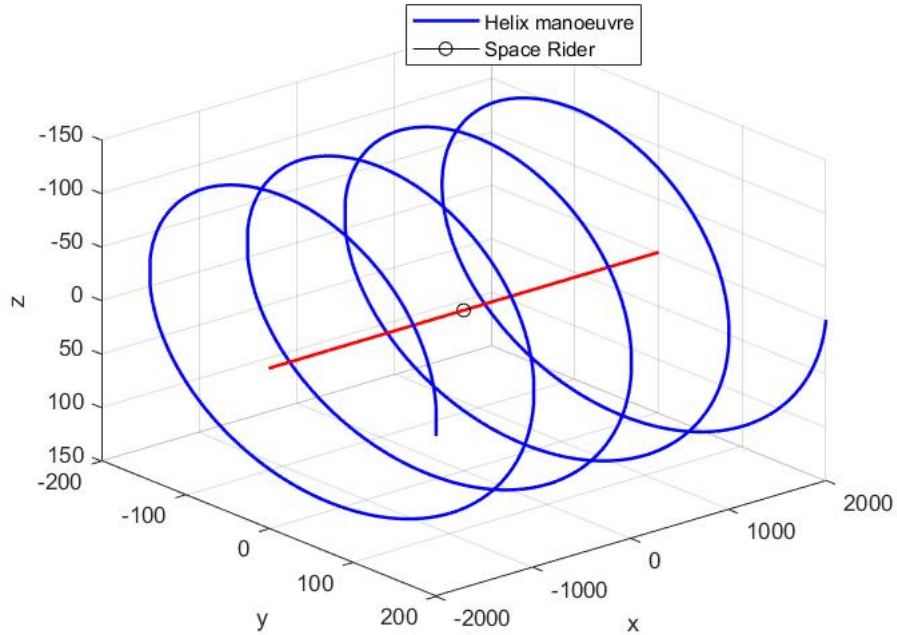


Figure 5.9: Helix manoeuvre (3.3) in four orbital periods (Table 5.2)

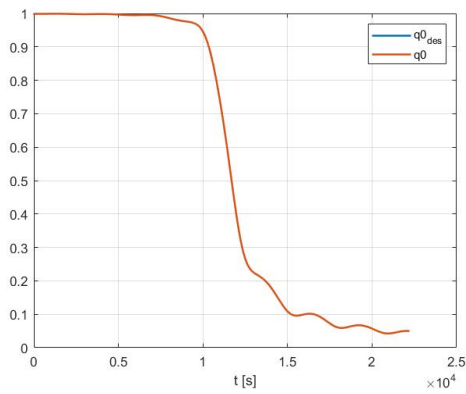


Figure 5.10: Temporal evolution of q_0 during tracking attitude control (Table 5.2)

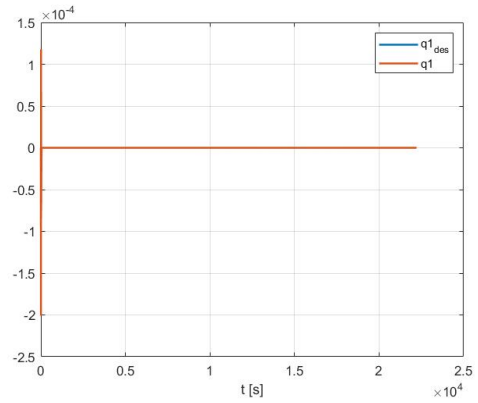


Figure 5.11: Temporal evolution of q_1 during tracking attitude control (Table 5.2)

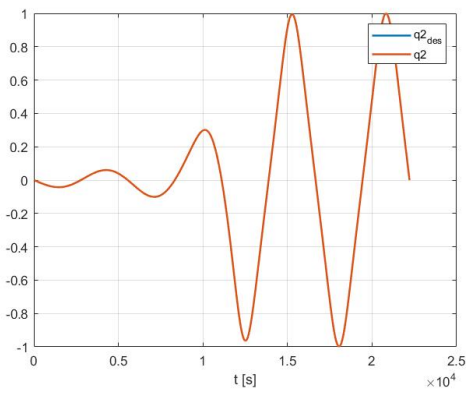


Figure 5.12: Temporal evolution of q_2 during tracking attitude control (Table 5.2)

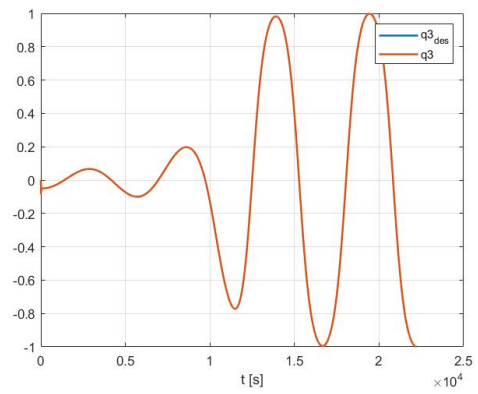


Figure 5.13: Temporal evolution of q_3 during tracking attitude control (Table 5.2)

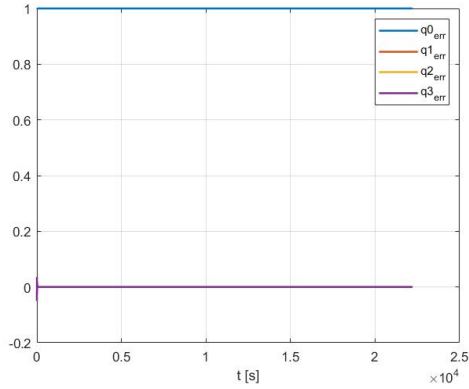


Figure 5.14: Temporal evolution of the quaternion error during tracking attitude control (Table 5.2)

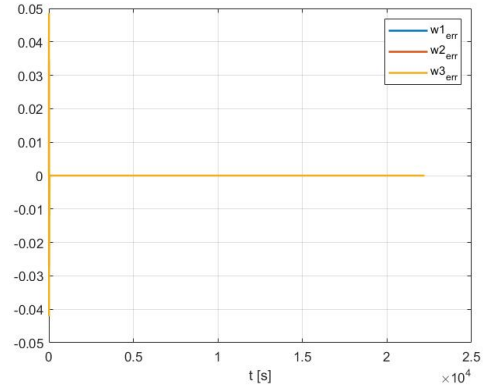


Figure 5.15: Temporal evolution of the angular velocity error during tracking attitude control (Table 5.2)

The results of both *case 1* (SROC orbits Space Rider clockwise) and *case 2* (SROC orbits Space Rider counterclockwise) show that the attitude tracking control is precisely carried out during the Helix manoeuvre. In fact, maximum *APE*, *MPE* and *RPE*, reported respectively in Table 5.3 and Table 5.4, are really small.

	Value	Measure of unit
<i>max APE</i>	0.0997	<i>rad</i>
<i>MPE</i>	$4.0486 \cdot 10^{-5}$	<i>rad</i>
<i>RPE</i>	0.0996	<i>rad</i>

Table 5.3: Case 1: *APE*, *MPE* and *RPE*

	Value	Measure of unit
<i>max APE</i>	0.0997	<i>rad</i>
<i>MPE</i>	$4.0601 \cdot 10^{-5}$	<i>rad</i>
<i>RPE</i>	0.0996	<i>rad</i>

Table 5.4: Case 2: *APE*, *MPE* and *RPE*

Furthermore, *APE* is less than 10^{-5} *rad* after only 40 *s* of the simulation, hence when SROC is still at a distance of about 1992 *m* from Space Rider. Moreover in Fig. 5.8 it is possible to see the high accuracy achieved by the Super-Twisting

SMC and also the strong attenuation of the chattering effect typical of the 1-order SMC (as said in section 2.2.3).

5.1.2 Helix manoeuvre (3.4)

Case 1

The Helix manoeuvre (3.4) carried out in four orbital periods (3.1) of Space Rider, with the initial conditions reported in Table 5.5, is depicted in Fig. 5.16.

Parameter	Value	Measure of unit
x_0	-2000	m
y_0	200	m
z_0	20	m
\dot{x}_0	0	m/s
\dot{y}_0	0	m/s
\dot{z}_0	5.2360	m/s
\vec{q}	$[1 \ 0 \ 0 \ 0]^T$	-
$\vec{\omega}$	$[0 \ 0 \ 0]^T$	rad/s

Table 5.5: Initial conditions of the simulation

Fig. 5.17 - 5.22 represent the temporal evolution of the quaternions, the quaternion error, that describes the pointing error, and also of the angular velocity error.

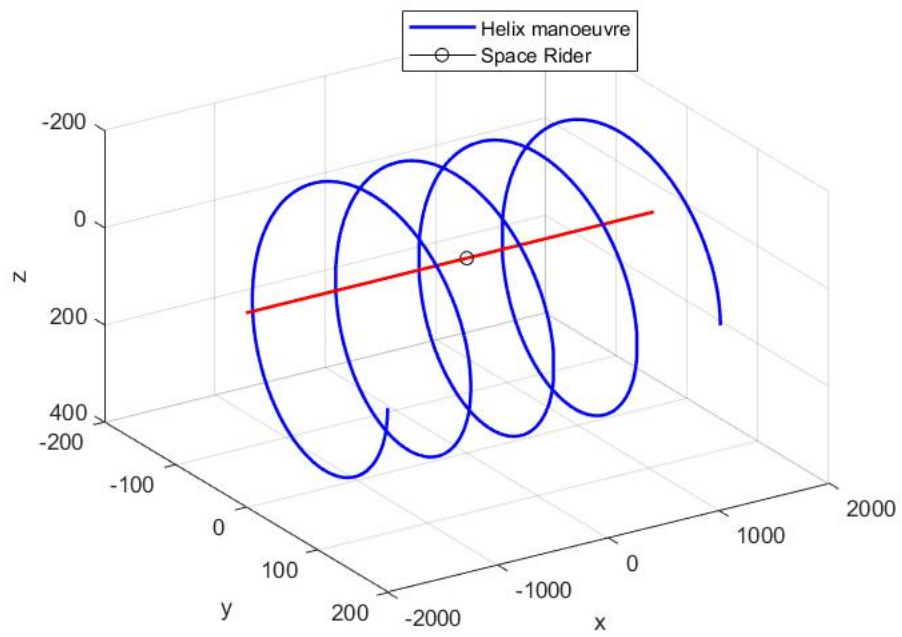


Figure 5.16: Helix manoeuvre (3.4) in four orbital periods (Table 5.5)

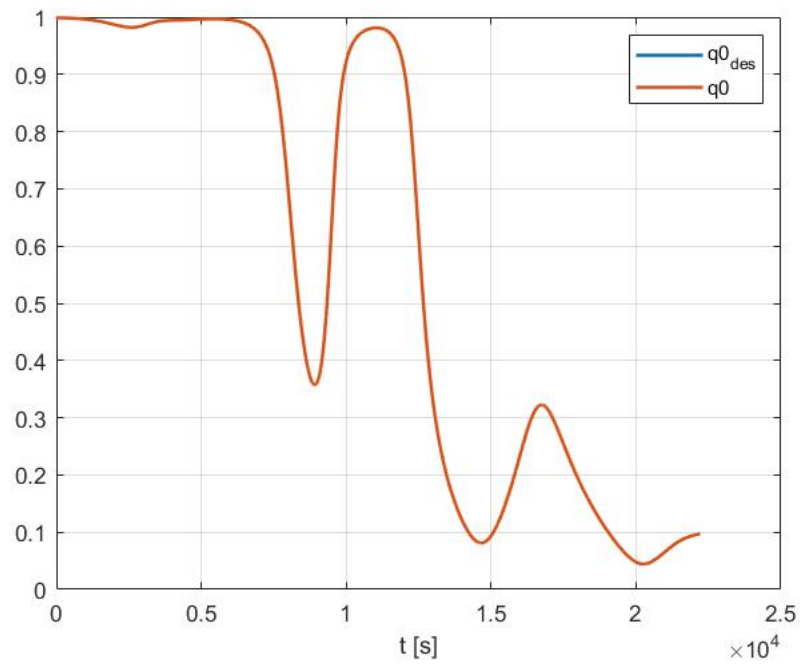


Figure 5.17: Temporal evolution of q_0 during tracking attitude control (Table 5.5)

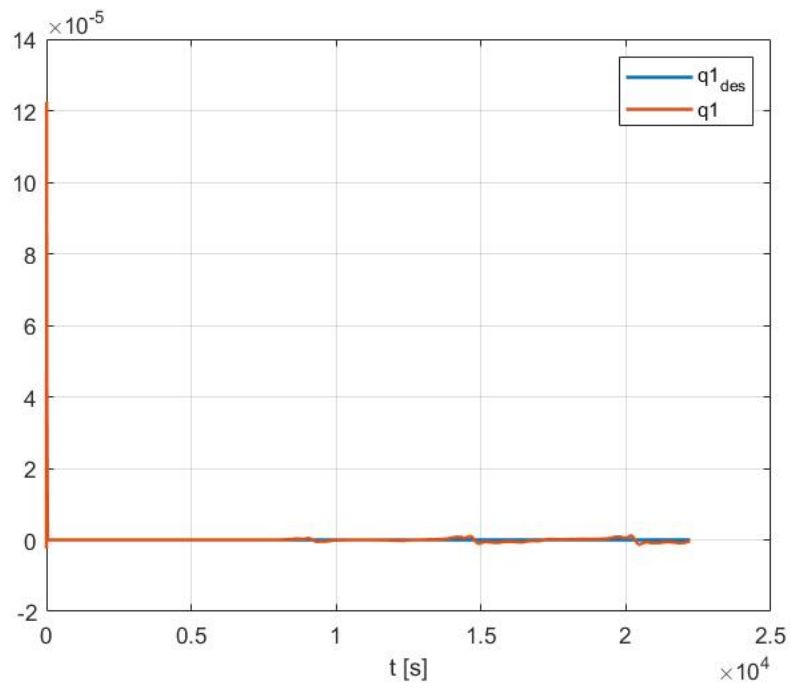


Figure 5.18: Temporal evolution of q_1 during tracking attitude control (Table 5.5)

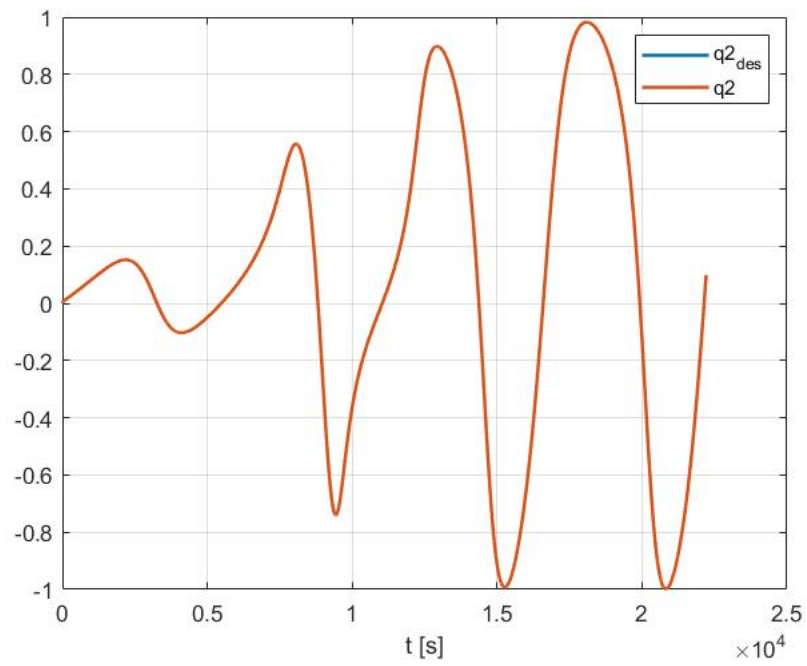


Figure 5.19: Temporal evolution of q_2 during tracking attitude control (Table 5.5)

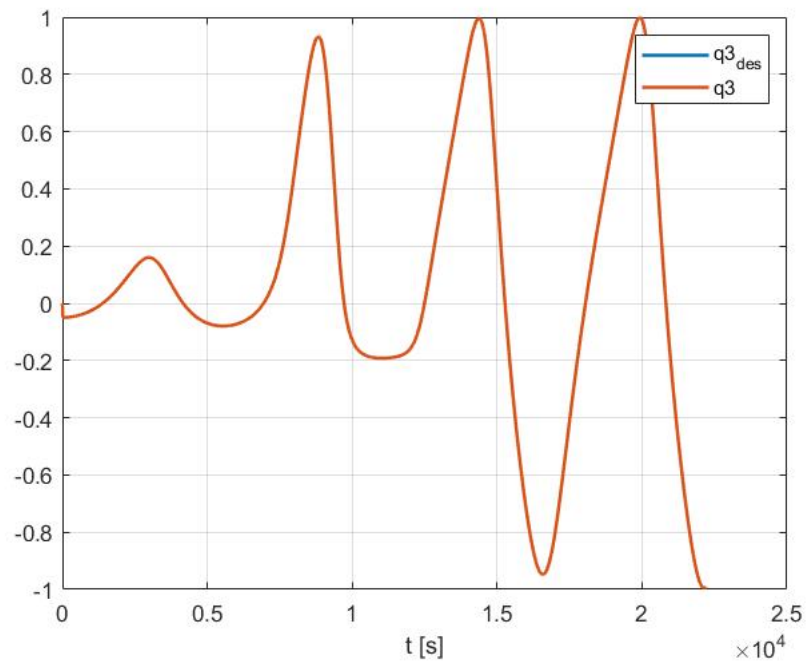


Figure 5.20: Temporal evolution of q_3 during tracking attitude control (Table 5.5)

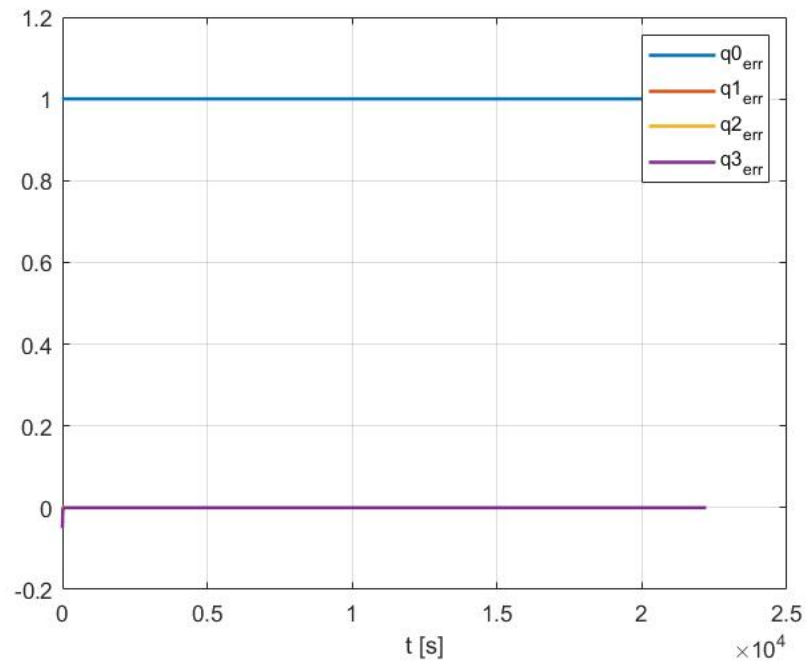


Figure 5.21: Temporal evolution of the quaternion error during tracking attitude control (Table 5.5)

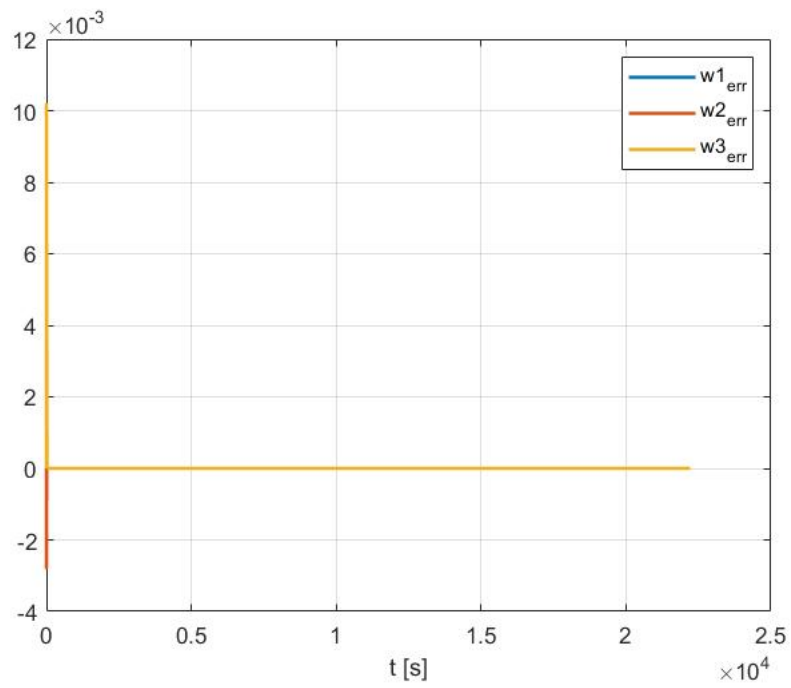


Figure 5.22: Temporal evolution of the angular velocity error during tracking attitude control (Table 5.5)

Case 2

If the initial conditions are those reported in Table 5.6, the Helix manoeuvre (3.4) carried out in four orbital periods (3.1) of Space Rider is depicted in Fig. 5.23, while Fig. 5.24 - 5.29 represent the temporal evolution of the quaternions, quaternion error and angular velocity error.

Parameter	Value	Measure of unit
x_0	-2000	m
y_0	-200	m
z_0	20	m
\dot{x}_0	0	m/s
\dot{y}_0	0	m/s
\dot{z}_0	5.2360	m/s
\vec{q}	$[1 \ 0 \ 0 \ 0]^T$	-
$\vec{\omega}$	$[0 \ 0 \ 0]^T$	rad/s

Table 5.6: Initial conditions of the simulation

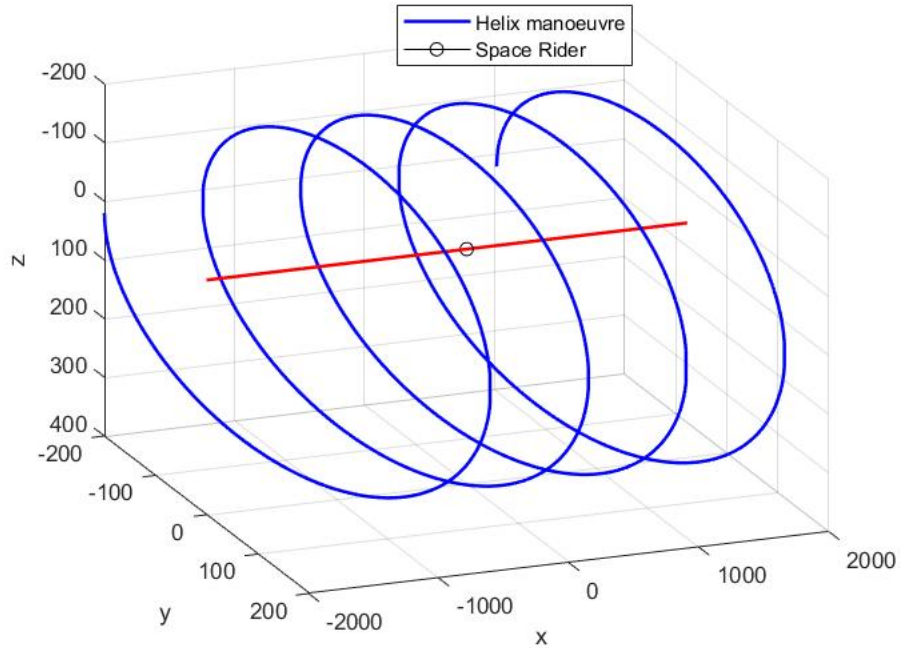


Figure 5.23: Helix manoeuvre (3.4) in four orbital periods (Table 5.6)

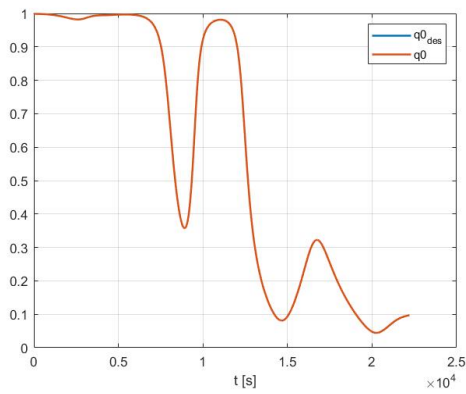


Figure 5.24: Temporal evolution of q_0 during tracking attitude control (Table 5.6)

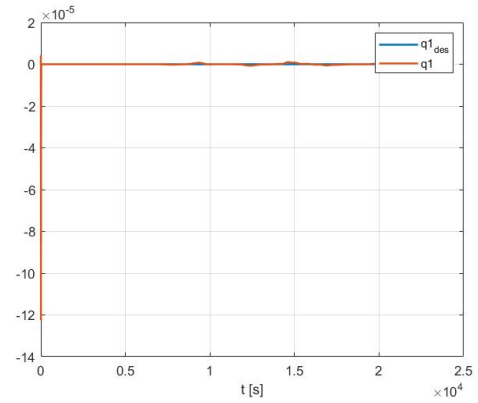


Figure 5.25: Temporal evolution of q_1 during tracking attitude control (Table 5.6)

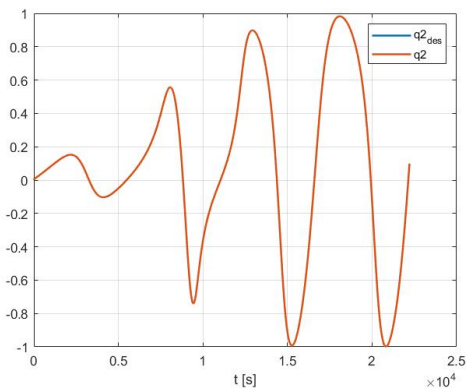


Figure 5.26: Temporal evolution of q_2 during tracking attitude control (Table 5.6)

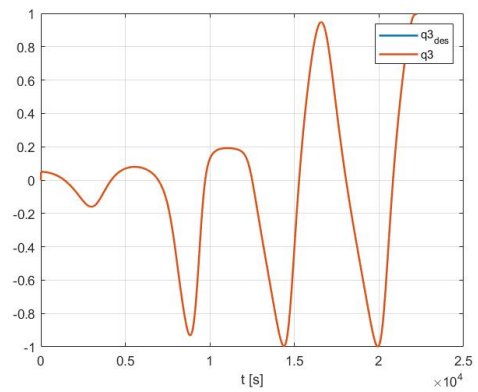


Figure 5.27: Temporal evolution of q_3 during tracking attitude control (Table 5.6)

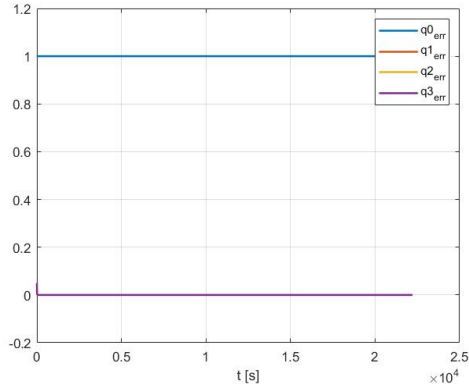


Figure 5.28: Temporal evolution of the quaternion error during tracking attitude control (Table 5.6)

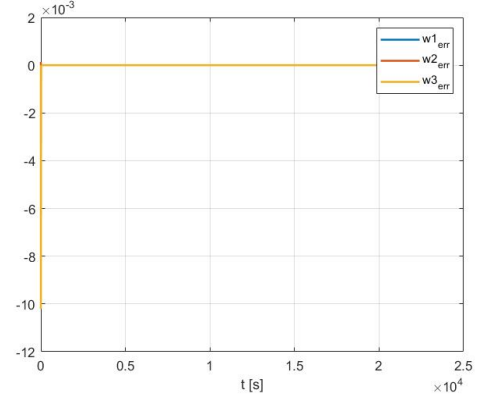


Figure 5.29: Temporal evolution of the angular velocity error during tracking attitude control (Table 5.6)

The results of both *case 1* (SROC orbits Space Rider clockwise) and *case 2* (SROC orbits Space Rider counterclockwise) show that the attitude tracking control is precisely carried out during the Helix manoeuvre. In fact, maximum *APE*, *MPE* and *RPE*, reported respectively in Table 5.7 and Table 5.8, are really small.

	Value	Measure of unit
<i>max APE</i>	0.1002	<i>rad</i>
<i>MPE</i>	$3.1264 \cdot 10^{-5}$	<i>rad</i>
<i>RPE</i>	0.1001	<i>rad</i>

Table 5.7: Case 1: *APE*, *MPE* and *RPE*

	Value	Measure of unit
<i>max APE</i>	0.1002	<i>rad</i>
<i>MPE</i>	$3.0864 \cdot 10^{-5}$	<i>rad</i>
<i>RPE</i>	0.1001	<i>rad</i>

Table 5.8: Case 2: *APE*, *MPE* and *RPE*

Furthermore, *APE* is less than 10^{-5} *rad* after only 40 *s* of the simulation, hence when SROC is still at a distance of about 1992 *m* from Space Rider.

Finally, it must be noted that the attitude guidance algorithm of section 3.2 is independent of the actual manoeuvre because it computes the reference vector from the real position of SROC in that instant. This is the reason why this attitude tracking control algorithm manages to adapt to "every" type of trajectory (as long as the right control gains are identified).

5.2 Monte Carlo simulation: nominal scenario

According to the initial conditions of Table 4.4, the robustness of the Super-Twisting SMC is verified through the results of 58 Monte Carlo simulations of the Helix manoeuvre (3.3). Fig. 5.30 - 5.32 show, respectively, the maximum APE , MPE and RPE , while the mean torques T_{mean} provided by the four Reaction Wheels are represented in Fig. 5.33. The results show that the MPE is always less than 1° and that the RWs effort is medium low. Furthermore, for the worst case ($\phi = \theta = \psi = 10^\circ$) APE is less than 1° after 650 s of the simulation, hence, when SROC is still at a distance of about 1883 m from Space Rider.

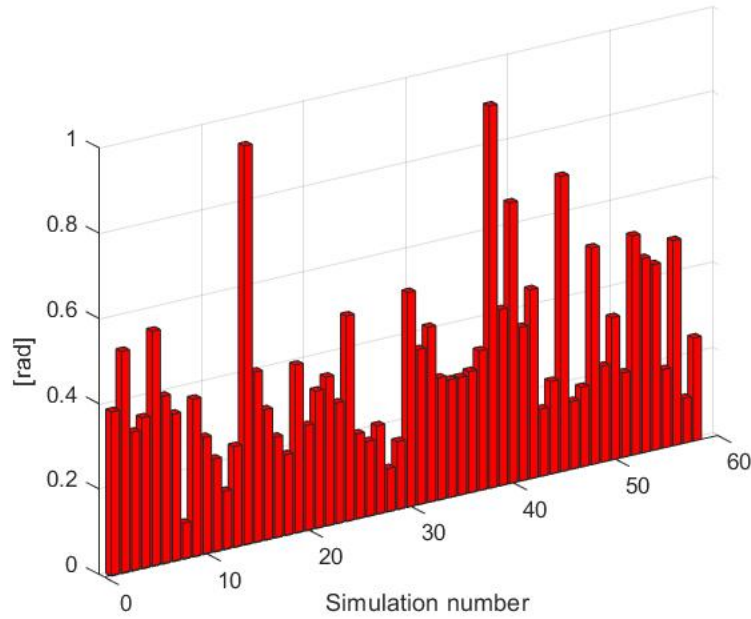


Figure 5.30: Maximum Absolute Performance Error (APE) over the 58 Monte Carlo simulations

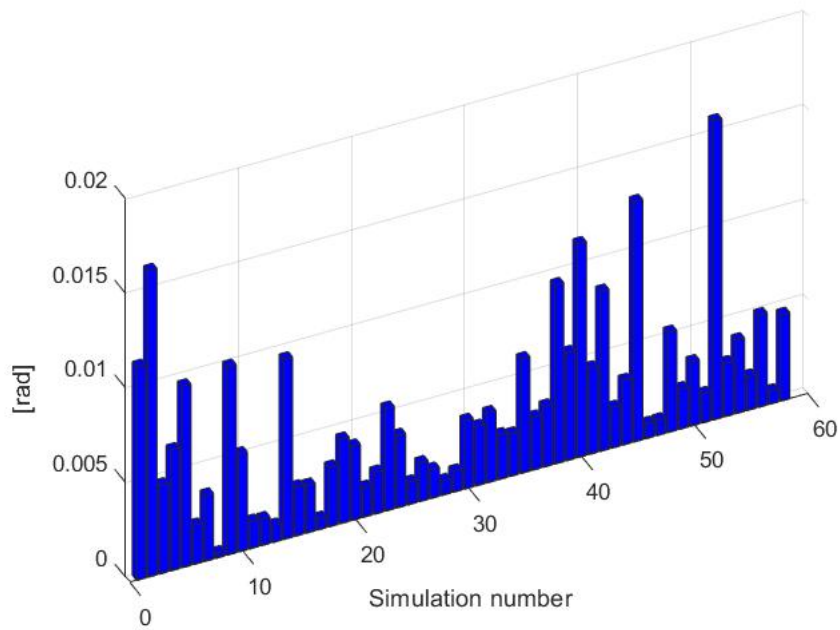


Figure 5.31: Mean Performance Error (MPE) over the 58 Monte Carlo simulations

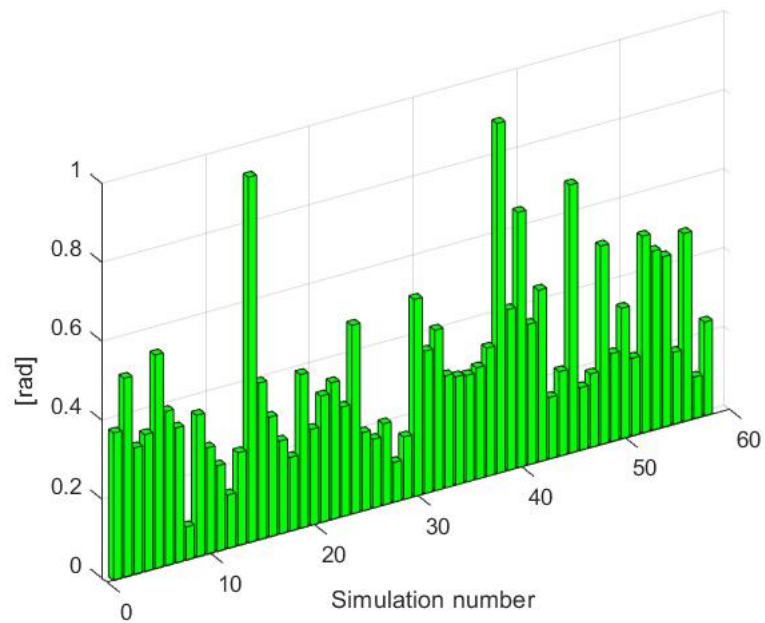


Figure 5.32: Relative Performance Error (RPE) over the 58 Monte Carlo simulations

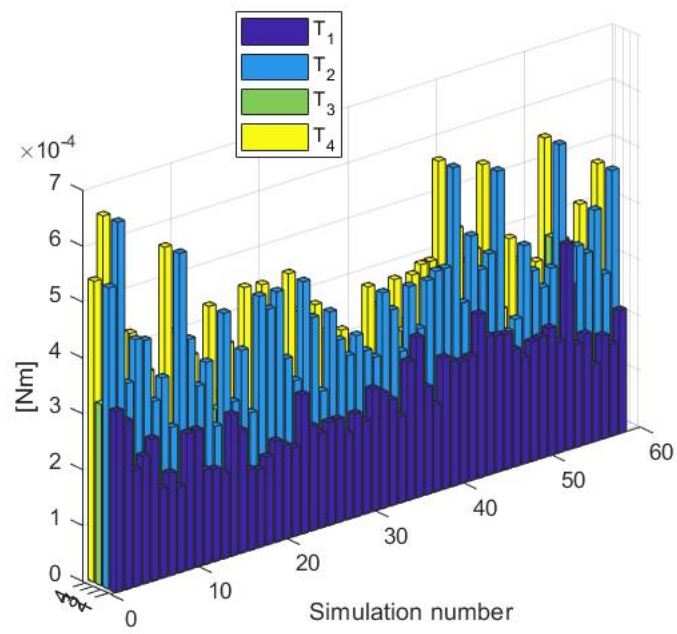


Figure 5.33: RWs mean torques T_{mean} over the 58 Monte Carlo simulations

5.3 Monte Carlo simulation: off-nominal scenario

Finally, according to the initial conditions of Table 4.4, the robustness of the Super-Twisting SMC is verified even in the case of casual failure of one of the four Reaction Wheels through the results of 120 Monte Carlo simulations of the Helix manoeuvre (3.3). Fig. 5.34 - 5.36 show, respectively, the maximum APE , MPE and RPE , while the mean torques T_{mean} provided by the four Reaction Wheels are represented in Fig. 5.37 (when the torque of a RW is null means that RW has a failure). The results show that the MPE is almost always very high (except for a few cases) and, consequently, the RWs effort is almost always maximum.

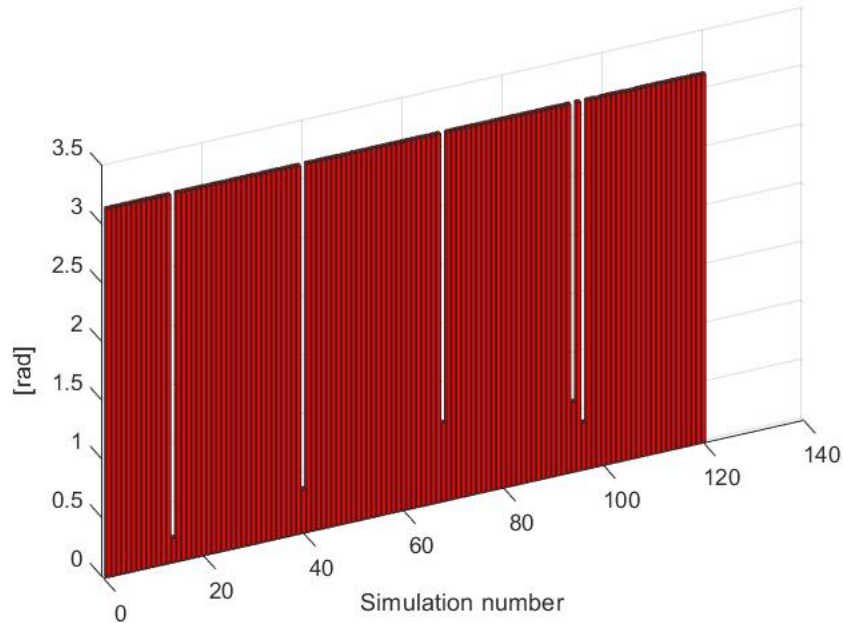


Figure 5.34: Maximum Absolute Performance Error (APE) over the 120 Monte Carlo simulations

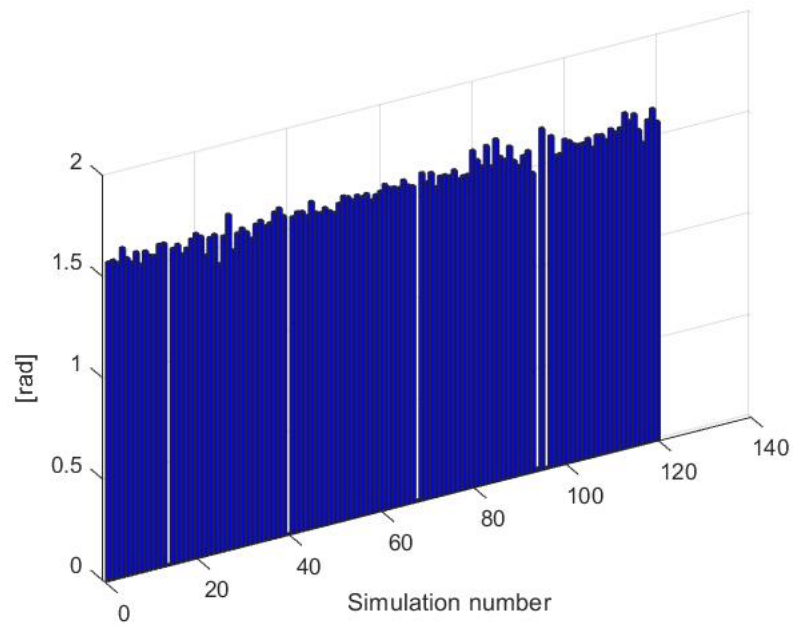


Figure 5.35: Mean Performance Error (MPE) over the 120 Monte Carlo simulations

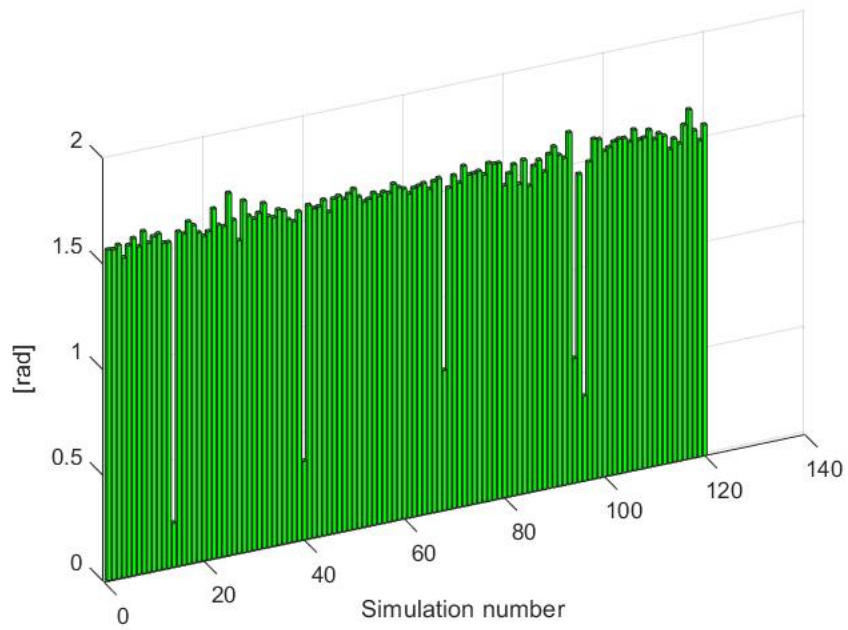


Figure 5.36: Relative Performance Error (RPE) over the 120 Monte Carlo simulations

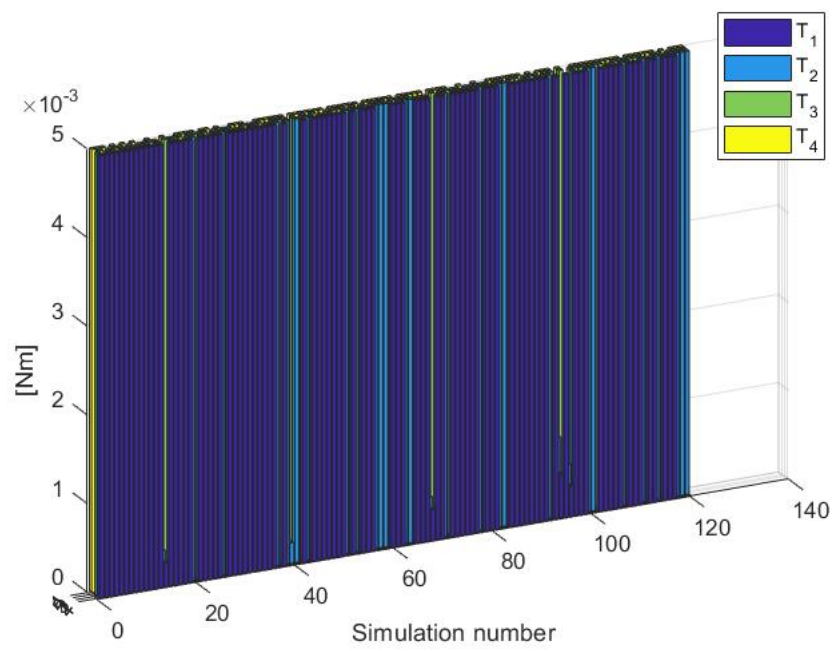


Figure 5.37: RWs mean torques T_{mean} over the 120 Monte Carlo simulations

Chapter 6

Model Predictive Control

6.1 Constrained LQ Finite Horizon optimal control

Considering a linear time-invariant (LTI) system in a discrete-state space representation

$$\begin{cases} x(k+1) = Ax(k) + Bu(k) \\ y(k) = Cx(k) + Du(k) \end{cases} \quad (6.1)$$

where $x(k)$ is the discrete-state space vector, $u(k)$ is the control action and $y(k)$ is the output of the system.

We define a Finite Horizon Cost Function

$$J = \sum_{i=0}^{H_p-1} x^T(k+i|k)Qx(k+i|k) + u^T(k+i|k)Ru(k+i|k) + x^T(k+H_p|k)Px(k+H_p|k) \quad (6.2)$$

where H_p is the prediction horizon, Q and R are the weighting matrices, P is the terminal weighting matrix, $x(k+i|k)$ is the state measurement at time k , and $u(k+i|k)$ is the control action at time given k . The goal is to find the optimal input (control action) sequence

$$U^*(k|k) = [u^*(k|k) \ u^*(k+1|k) \ \dots \ u^*(k+H_p-1|k)]^T \quad (6.3)$$

that minimizes J . In order to set the optimization problem in a quadratic formulation [39, 40],

where

$$H = 2(\bar{R} + \bar{S}^T \bar{Q} \bar{S})$$

$$F = 2(\bar{T}^T \bar{Q} \bar{S})$$

while u_{min} , u_{max} , x_{min} and x_{max} are the constraints of the control action and of the state space.

However, even in the constrained case, the application of the minimizing sequence (6.3), gives rise to an open loop control strategy that is affected by uncertainty and disturbances. Such a problem is addressed by a feedback control strategy that is realized through the Receding Horizon (RH) principle, that is defined by the recursive procedure below [40]:

At sampling instant k

1. get the state $x(k) = x(k|k)$
2. solve the considered QP optimization problem (6.4) w.r.t. $U(k|k)$
3. compute the minimizer $U(k|k)^*$
4. apply, as present control action, $u(k) = u(k|k)^*$ (i.e. the first element only of the minimizer, the others are discarded).

6.2 Tracking MPC

If the state space has to track a reference $r(k)$, the output tracking can be accounted for by including in the cost function (6.2) a quadratic term of the tracking error $x(k+i|k) - r(k+i|k)$:

$$J = \sum_{i=0}^{H_p-1} (x(k+i|k) - r(k+i|k))^T Q (x(k+i|k) - r(k+i|k)) + u^T(k+i|k) R u(k+i|k) \quad (6.6)$$

Hence, the linear quadratic (LQ) constrained optimization problem becomes [39, 40]:

$$B = \begin{bmatrix} 0^{3,3} \\ J^{-1} \end{bmatrix} \quad (6.14)$$

with

$$A_{11} = \begin{bmatrix} 0 & 0 & 0 & 0 \\ 0 & 0 & 0 & 0 \\ 0 & 0 & 0 & 0 \\ 0 & 0 & 0 & 0 \end{bmatrix} \quad (6.15)$$

$$A_{12} = \frac{1}{2} \begin{bmatrix} -q_1 & -q_2 & -q_3 \\ q_0 & -q_3 & q_2 \\ q_3 & q_0 & -q_1 \\ -q_2 & q_1 & q_0 \end{bmatrix} \quad (6.16)$$

$$A_{21} = \begin{bmatrix} 0 & 0 & 0 & 0 \\ 0 & 0 & 0 & 0 \\ 0 & 0 & 0 & 0 \end{bmatrix} \quad (6.17)$$

$$A_{22} = \begin{bmatrix} 0 & 0 & 0 \\ 0 & 0 & 0 \\ 0 & 0 & 0 \end{bmatrix} \quad (6.18)$$

$0^{3,3}$ null matrix and J inertia matrix.

In our case the reference vector (6.8) is, at sampling instant k ,

$$r(k) = [q_{r_0} \ q_{r_1} \ q_{r_2} \ q_{r_3} \ \omega_{r_x} \ \omega_{r_y} \ \omega_{r_z}]^T \quad (6.19)$$

where $\vec{q}_r = [q_{r_0} \ q_{r_1} \ q_{r_2} \ q_{r_3}]^T$ and $\vec{\omega}_r = [\omega_{r_x} \ \omega_{r_y} \ \omega_{r_z}]^T$ are, respectively, the reference quaternion (3.12) and the reference angular velocity (3.15) computed in section 3.2.

6.4 Simulations and results

In this section the results of the tracking MPC are presented. The prediction horizon H_p and the weighting matrices Q , R , and P , identified through the try and error process based on simulation sessions, have the following values:

$$H_p = 5$$

$$Q = \begin{bmatrix} 10^5 & 0 & 0 & 0 & 0 & 0 & 0 \\ 0 & 10^5 & 0 & 0 & 0 & 0 & 0 \\ 0 & 0 & 10^5 & 0 & 0 & 0 & 0 \\ 0 & 0 & 0 & 10^5 & 0 & 0 & 0 \\ 0 & 0 & 0 & 0 & 10^5 & 0 & 0 \\ 0 & 0 & 0 & 0 & 0 & 10^5 & 0 \\ 0 & 0 & 0 & 0 & 0 & 0 & 10^5 \end{bmatrix}$$

$$R = \begin{bmatrix} 10^{-50} & 0 & 0 \\ 0 & 10^{-50} & 0 \\ 0 & 0 & 10^{-50} \end{bmatrix}$$

$$P = \begin{bmatrix} 10^5 & 0 & 0 & 0 & 0 & 0 & 0 \\ 0 & 10^5 & 0 & 0 & 0 & 0 & 0 \\ 0 & 0 & 10^5 & 0 & 0 & 0 & 0 \\ 0 & 0 & 0 & 10^5 & 0 & 0 & 0 \\ 0 & 0 & 0 & 0 & 10^5 & 0 & 0 \\ 0 & 0 & 0 & 0 & 0 & 10^5 & 0 \\ 0 & 0 & 0 & 0 & 0 & 0 & 10^5 \end{bmatrix}$$

If the initial conditions are those reported in Table 5.1, the Helix manoeuvre (3.3) carried out in four orbital periods (3.1) of Space Rider is depicted in Fig. 5.1, while Fig. 6.1 - 6.4 represent the temporal evolution of the quaternions. It is evident that the tracking MPC does not manage to follow the reference quaternion.

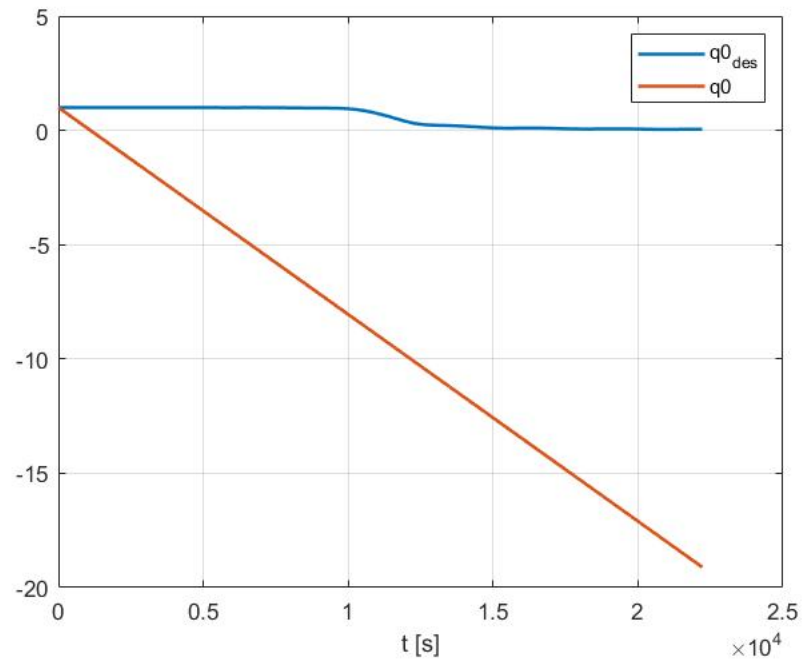


Figure 6.1: Temporal evolution of q_0 during tracking attitude control

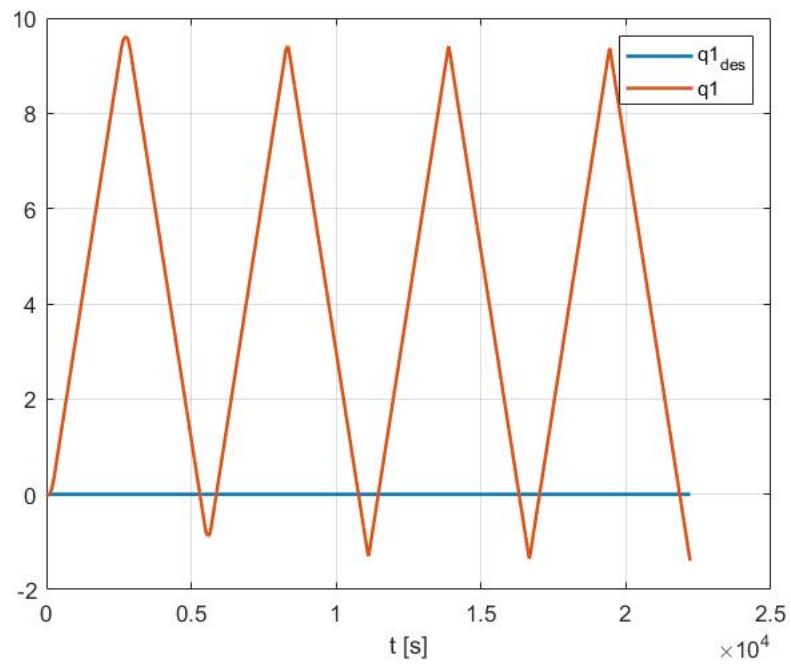


Figure 6.2: Temporal evolution of q_1 during tracking attitude control

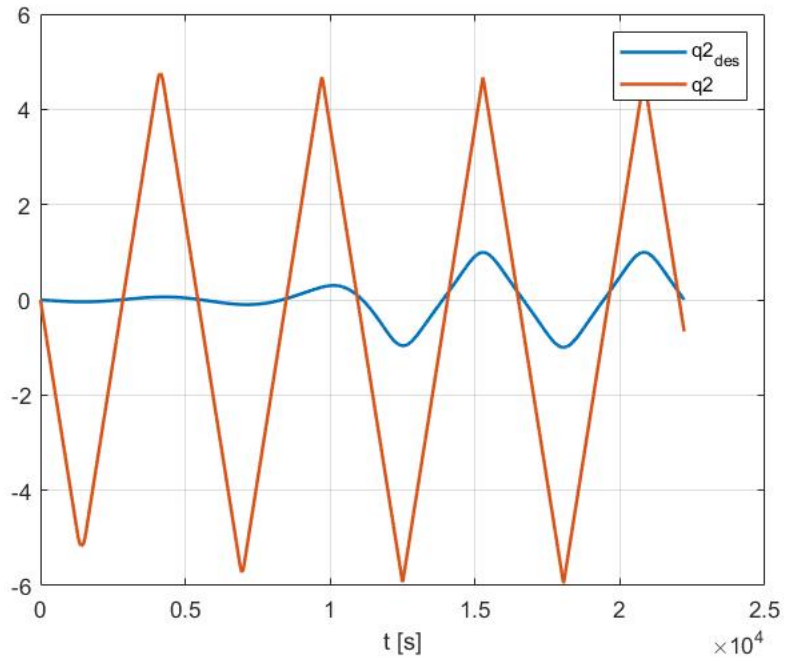


Figure 6.3: Temporal evolution of q_2 during tracking attitude control

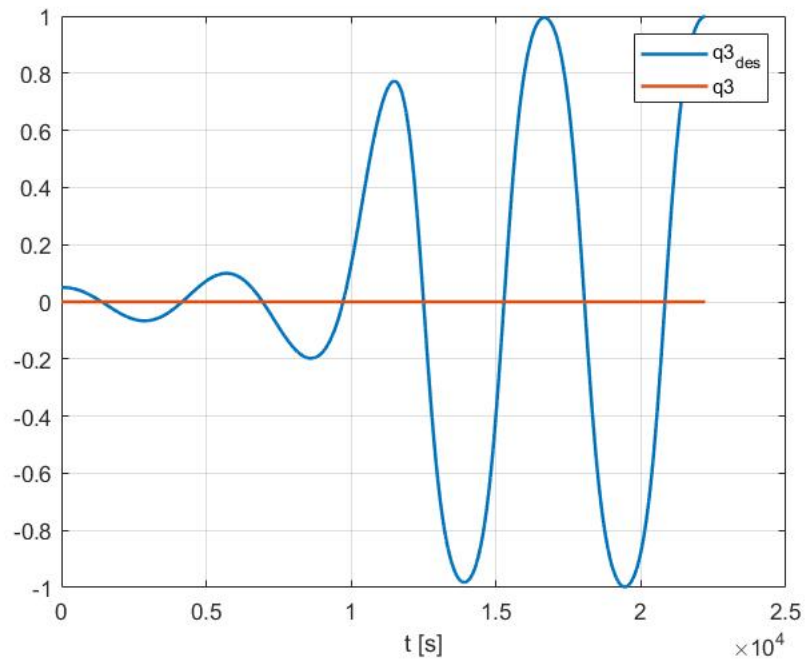


Figure 6.4: Temporal evolution of q_3 during tracking attitude control

Chapter 7

Conclusions

The main objective of the thesis is to define guidance and control strategies for small satellites involved in the observation/inspection of a collaborative target. For the attitude guidance it has been used a method based on computing, in each position of the trajectory, the Euler axis to correctly point to the center of mass of Space Rider. The simulations conducted for four different trajectories of SROC show that this algorithm is independent of the actual manoeuvre because it computes the reference vector from the real position of SROC in that instant. For the attitude tracking control a Super-Twisting Sliding Mode Control has been designed. The Monte Carlo simulations demonstrate its high accuracy and its robustness against the uncertainties of the parameters of the satellite, besides the strong attenuation of the chattering effect typical of the 1-order SMC. However, section 5.3 highlights that the proposed Super-Twisting SMC is not robust in the case of a casual failure of one of the four Reaction Wheels. Therefore, it might be useful to tune the controller for this off-nominal scenario.

The next step will be the integration of all the blocks concerning sensors and navigation filter, besides a more detailed external disturbances and CubeSat model, in the orbital simulator.

Chapter 6 introduces the Model Predictive Control, hence, future researches might be focused on a better implementation of an this controller.

Appendix A

Reference frames

A.1 Earth centered inertial frame

The Earth centered inertial (ECI) or Geocentric-equatorial system has its origin at the Earth's center. The fundamental plane is the equator and the positive X -axis points in the vernal equinox direction (towards the constellation of Ares), the Z -axis points in the direction of the north pole and the Y -axis finishes the triad of the reference system and it's in the equatorial plane. It is important to keep in mind when looking at Fig. A.1 that the XYZ system is not fixed to the Earth and turning with it; rather, the Geocentric-equatorial frame is nonrotating wrt the stars (except for precession of the equinoxes) and the Earth turns relative to it [41].

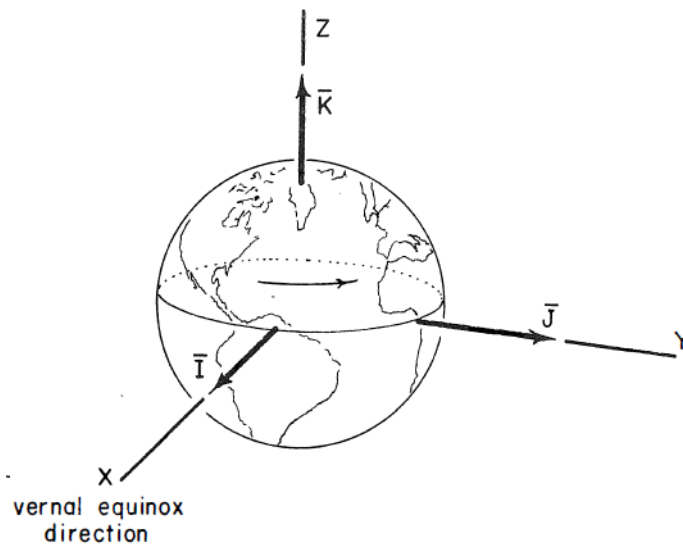


Figure A.1: Earth inertial frame [41]

A.2 Body reference frame

The origin of the body reference frame is fixed at the spacecraft's center of mass, and its axis corresponds to the main direction of inertia, but normally, they can be adjusted depending on the mission phase. In contrast to the inertial reference frame, this one moves with the spacecraft, and by making an appropriate comparison with it, it is possible to determine the attitude angles.

A.3 LVLH frame

The Local Vertical Local Horizontal (LVLH) frame is a local reference system attached to the target spacecraft (as shown in Fig. A.1). R_{bar} axis is along the vertical line towards the Earth center, V_{bar} is in the direction of orbital motion parallel to the local horizontal and H_{bar} is perpendicular to the orbital plane, opposite direction wrt angular momentum. The LVLH frame rotates with angular velocity vector ω and its current orientation with respect to the ECI frame is given by a rotation matrix appropriately defined.

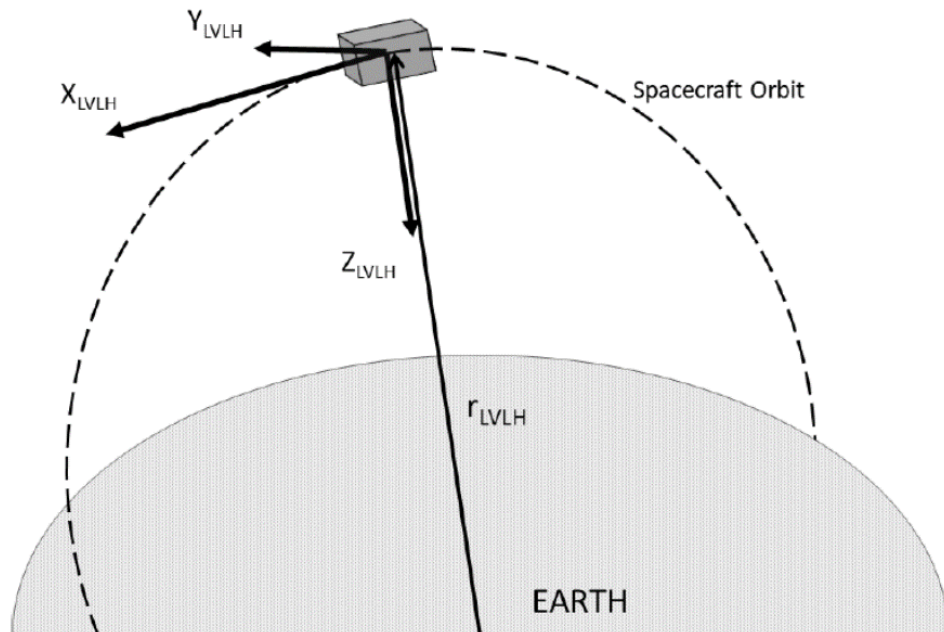


Figure A.2: LVLH frame [33]

Appendix B

Euler angles

Assuming that a satellite is a rigid body, we can attach to it a body frame, F_B , described by a set of unit vectors $(\hat{e}_1, \hat{e}_2, \hat{e}_3)$. The position of F_B with respect to an inertial reference frame F_I (LVLH frame), identified by the unit vectors $(\hat{E}_1, \hat{E}_2, \hat{E}_3)$, completely describes the attitude of a spacecraft. Assuming that \vec{v} is a vector quantity, it is possible to write it as

$$\vec{v} = x\hat{e}_1 + y\hat{e}_2 + z\hat{e}_3$$

or, equivalently,

$$\vec{v} = X\hat{E}_1 + Y\hat{E}_2 + Z\hat{E}_3$$

The column vectors $\vec{v}_B = (x, y, z)^T$ and $\vec{v}_I = (X, Y, Z)^T$ provide the component representations of the same vector quantity \vec{v} in the reference frames F_B and F_I , respectively [42]. It is possible to write

$$\vec{v}_B = [L_{BI}]\vec{v}_I \tag{B.1}$$

where $[L_{BI}]$ is the rotation matrix from the LVLH frame to the body one. It is possible to use $[L_{BI}]$ to describe the attitude of the spacecraft through the unit vectors \hat{e}_i of the body frame attached to it, coming out with a total of 9 parameters. One of the set of three parameters most widely used to describe the attitude of a rigid body (or equivalently the attitude of the body frame attached to it) wrt a fixed frame are the Euler's angles, a sequence of three rotations that take the fixed frame and make it coincide with the body frame. The original sequence of rotations proposed by Euler to superimpose F_I onto F_B is the sequences 3-1-3:

1. the first rotation is about the third axis of the initial frame, that is \hat{E}_3 and takes the first axis \hat{E}_1 to the direction \hat{e}'_1 perpendicular to the plane determined

by the unit vectors \hat{E}_3 and \hat{e}_3 ; \hat{E}_2 is rotated onto \hat{e}'_2 ; the rotation angle is called precession angle Ψ

2. the second rotation is about the first axis transformed after the first rotation, \hat{e}'_1 , and takes the axis \hat{e}'_3 into the position of \hat{e}_3 ; \hat{e}'_2 is moved onto \hat{e}''_2 ; the rotation angle is called nutation angle Θ ;
3. the third and final rotation is about \hat{e}_3 and brings $\hat{e}''_1 = \hat{e}'_1$ and \hat{e}''_2 to their final positions, \hat{e}_1 and \hat{e}_2 , respectively; the rotation angle is called spin angle Φ .

The three angles, representing the amplitude of the three successive rotations Ψ, Θ, Φ respectively about the third, the first, and again the third axis, can be used to represent the attitude of the frame F_B . The transformation matrix L_{BI} can be expressed as a function of these three angles, in terms of three elementary rotation matrices [42].

The coordinate transformation during the first rotation is given by

$$\begin{Bmatrix} x' \\ y' \\ z' \end{Bmatrix} = \begin{bmatrix} \cos(\Psi) & \sin(\Psi) & 0 \\ -\sin(\Psi) & \cos(\Psi) & 0 \\ 0 & 0 & 1 \end{bmatrix} \begin{Bmatrix} X \\ Y \\ Z \end{Bmatrix}$$

during the second rotation

$$\begin{Bmatrix} x'' \\ y'' \\ z'' \end{Bmatrix} = \begin{bmatrix} 1 & 0 & 0 \\ 0 & \cos(\Theta) & \sin(\Theta) \\ 0 & -\sin(\Theta) & \cos(\Theta) \end{bmatrix} \begin{Bmatrix} x' \\ y' \\ z' \end{Bmatrix}$$

and during the third rotation

$$\begin{Bmatrix} x \\ y \\ z \end{Bmatrix} = \begin{bmatrix} \cos(\Phi) & \sin(\Phi) & 0 \\ -\sin(\Phi) & \cos(\Phi) & 0 \\ 0 & 0 & 1 \end{bmatrix} \begin{Bmatrix} x'' \\ y'' \\ z'' \end{Bmatrix}$$

The three elementary rotation matrices of the Euler's sequence 3-1-3 can thus be defined as

$$[R_3(\Psi)] = \begin{bmatrix} \cos(\Psi) & \sin(\Psi) & 0 \\ -\sin(\Psi) & \cos(\Psi) & 0 \\ 0 & 0 & 1 \end{bmatrix}$$

$$[R_1(\Theta)] = \begin{bmatrix} 1 & 0 & 0 \\ 0 & \cos(\Theta) & \sin(\Theta) \\ 0 & -\sin(\Theta) & \cos(\Theta) \end{bmatrix}$$

$$[R_3(\Phi)] = \begin{bmatrix} \cos(\Phi) & \sin(\Phi) & 0 \\ -\sin(\Phi) & \cos(\Phi) & 0 \\ 0 & 0 & 1 \end{bmatrix}$$

When passing from the inertial frame F_I to the body frame F_B using Euler's sequence, the coordinate transformation of vector quantities can be obtained combining in the correct order the elementary rotation matrices, as follows:

$$\vec{v}_B = [R_3(\Phi)][R_1(\Theta)][R_3(\Psi)] \vec{v}_I \quad (\text{B.2})$$

This means that

$$[L_{BI}] = [R_3(\Phi)][R_1(\Theta)][R_3(\Psi)] \quad (\text{B.3})$$

Appendix C

Quaternions

C.1 Euler's axis rotation theorem

Euler's axis rotation theorem states that it is possible to rotate a frame F_1 onto any arbitrary frame F_2 with a simple rotation α around an axis \vec{a} that is fixed in both frames (Fig. C.1), called the Euler's rotation axis, the direction cosines of which are the same in the two considered frame. If the objective is to rotate the fixed frame F_I onto any arbitrary frame F_B , the transformation matrix $[L_{BI}]$ is a function of the Euler axis \vec{a} and the angle of rotation α :

$$[L_{BI}] = \cos\alpha I + (1 - \cos\alpha)\vec{a}\vec{a}^T - \sin\alpha A \quad (\text{C.1})$$

where I is the identity matrix and

$$A = \begin{bmatrix} 0 & -a_3 & a_2 \\ a_3 & 0 & -a_1 \\ -a_2 & a_1 & 0 \end{bmatrix} \quad (\text{C.2})$$

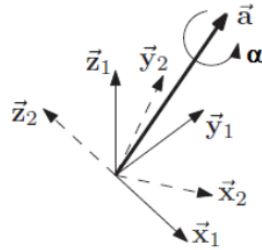


Figure C.1: Euler's axis rotation theorem [33]

We now define the Euler parameters or quaternions as

$$\begin{cases} q_0 = \cos(\frac{\alpha}{2}) \\ q_1 = a_1 \sin(\frac{\alpha}{2}) \\ q_2 = a_2 \sin(\frac{\alpha}{2}) \\ q_3 = a_3 \sin(\frac{\alpha}{2}) \end{cases} \quad (C.3)$$

Therefore, the the transformation matrix $[L_{BI}]$ becomes:

$$[L_{BI}] = (q_0^2 - \vec{q}_v \cdot \vec{q}_v)I + 2\vec{q}_v \vec{q}_v^T - 2q_0Q \quad (C.4)$$

where $\vec{q}_v = [q_1 \ q_2 \ q_3]^T$ and q_0 are, respectively, the vectorial part and the scalar part of the quaternion q and

$$A = \begin{bmatrix} 0 & -q_3 & q_2 \\ q_3 & 0 & -q_1 \\ -q_2 & q_1 & 0 \end{bmatrix} \quad (C.5)$$

In comparison to Euler's angles, the quaternions have a number of benefits, chief among them the absence of inherent geometric singularity. Also, compared to the equation derived for the Euler's angles, the linear equation that must be integrated over time to calculate their evolution as a function of angular velocity components is computationally less expensive. The cost is that four independent factors are used rather than just three. Another disadvantage is that, unlike Euler's angles, which have an intuitive geometric meaning, their geometric interpretation during an evolution is less immediate. The quaternion multiplication process, however, enables a strict characterization of misalignment errors that is otherwise impossible to get [42].

C.2 The quaternion error vector

Assume that the current attitude of a frame F_B associated with a rigid body with respect to a given fixed frame F_I is represented by the quaternion q , while q_{des} represent the desired attitude F_D of the body. The magnitude of the angular displacement between F_B and F_D , represented by the amplitude ϵ of the eigenaxis rotation around \hat{a} that takes F_D onto F_B , can be seen as the "error" in the current attitude with respect to the desired one. Provided that the rotation that takes F_I onto F_D can be combined with that that takes F_D onto F_B , it is possible to assess by means of the quatenion operation that

$$\vec{q} \otimes \vec{q}_{err} = \vec{q}_{des}$$

where $\vec{q}_{err} = [q_{err_0} \vec{q}_{err_v}]^T$ is the quaternion error, that is the quaternion associated with the rotation that takes F_B onto F_D , the amplitude of which thus provides the misalignment error of F_D with respect to F_B [42]. By pre-multiplication of both terms by the conjugate quaternion \vec{q}^* one gets

$$\vec{q}_{err} = \vec{q}^* \otimes \vec{q}_{des} = \begin{bmatrix} q^*_0 & -q^*_1 & -q^*_2 & -q^*_3 \\ q^*_1 & q^*_0 & -q^*_3 & -q^*_2 \\ q^*_2 & q^*_3 & q^*_0 & -q^*_1 \\ q^*_3 & -q^*_2 & q^*_1 & q^*_0 \end{bmatrix} \begin{bmatrix} q_{des_0} \\ q_{des_1} \\ q_{des_2} \\ q_{des_3} \end{bmatrix} \quad (C.6)$$

where

$$\vec{q}^* = [q_0 \ -q_1 \ -q_2 \ -q_3]^T \quad (C.7)$$

Appendix D

Impulsive manoeuvres

As a first approximation, thrust manoeuvres can be thought of as impulses, or momentaneous changes in velocity, during the time of the maneuver. Such perfect impulsive maneuvers do not actually exist due to the limited thrust levels that are accessible; instead, constant thrust forces must be delivered over a specific period of time to realize the maneuver [35].

D.1 Radial boost

Thrust manoeuvres with a ΔV in $\pm z$ direction (LVLH frame) can be used for transfer along the target orbit and for fly-around to an R-bar approach. A particular property of radial manoeuvres is that they affect only the eccentricity, not the orbital period, and thus cause no drift wrt the target orbit [35].

Fig. D.1 shows the application of two ΔV in a radial direction for a transfer to a different position on the target orbit. Starting at x_1 , the transfer time to x_2 is half an orbital period. To stop the motion at x_2 , an impulse of the same size and direction, $\Delta V_{z_1} = \Delta V_{z_2}$, must be applied. With $\Delta x = x_2 - x_1$ the required ΔV in both cases becomes:

$$\Delta V_{z_1} = \Delta V_{z_2} = \frac{\omega}{4} \Delta x \tag{D.1}$$

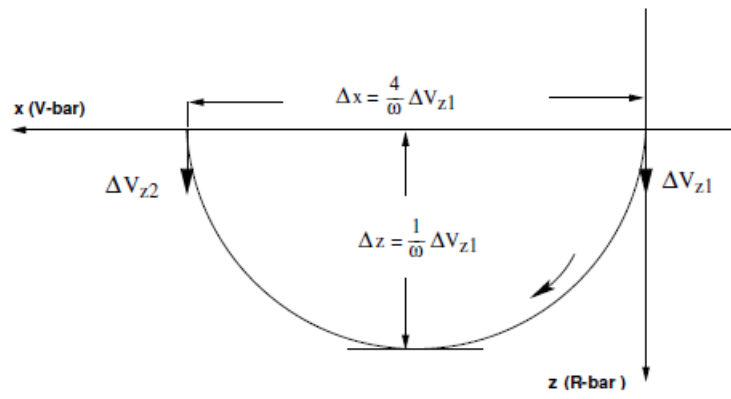


Figure D.1: Transfer along V-bar by radial impulses [35]

D.2 Motion in the y direction

Considering the following initial conditions

$$\begin{cases} x_0 = z_0 = 0 \\ y_0 = Y_0 \\ \dot{x}_0 = \dot{y}_0 = \dot{z}_0 = 0 \end{cases} \quad (\text{D.2})$$

and inserting into the Hill's equations (3.4), the equations of motion are:

$$\begin{cases} x(t) = 0 \\ y(t) = Y_0 \cos(\omega t) \\ z(t) = 0 \end{cases} \quad (\text{D.3})$$

The result is the expected pure sinusoidal motion starting with Y_0 (Fig. D.2). As this motion is de-coupled from the in-plane motions, this result can be superimposed to all in-plane cases [35].

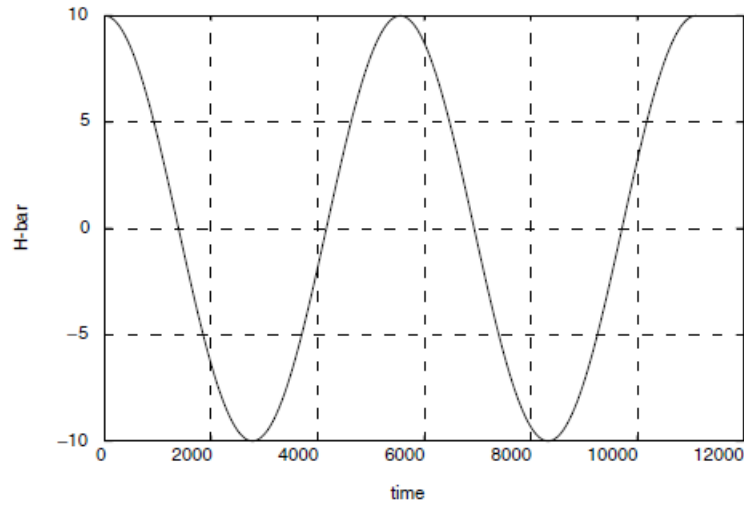


Figure D.2: Motion over time after release at an out-of-plane distance of $Y_0 = 10 \text{ m}$ [35]

Bibliography

- [1] Z. Feng and J. Fei. «Design and analysis of adaptive supertwisting sliding mode control for a microgyroscope». In: (2018) (cit. on p. 2).
- [2] Z. Feng and J. Fei. «Adaptive integral-type terminal sliding mode fault tolerant control for spacecraft attitude tracking». In: (2019) (cit. on p. 2).
- [3] G. Sun et al. «Practical tracking control of linear motor via fractional-order sliding mode». In: (2018) (cit. on p. 2).
- [4] L. Wang and Z. Song. «Continuous fixed-time sliding mode attitude controller design for rigid-body spacecraft». In: (2020) (cit. on p. 2).
- [5] L. Luque-Vega et al. «Robust block second order sliding mode control for a quadrotor». In: (2012) (cit. on p. 2).
- [6] F. Chen et al. «Robust backstepping sliding-mode control and observer-based fault estimation for a quadrotor uav». In: (2016) (cit. on p. 2).
- [7] D. Almakhlles. «Robust backstepping sliding mode control for a quadrotor trajectory tracking application». In: (2019) (cit. on p. 2).
- [8] F. Bayat. «Model predictive sliding control for finite-time three-axis spacecraft attitude tracking». In: (2018) (cit. on p. 2).
- [9] Yuri Shtessel et al. «Sliding mode control and observation». In: (2014) (cit. on pp. 3, 9–11, 13–20).
- [10] Y. B. Shtessel et al. «Super-twisting adaptive sliding mode control: a lyapunov design». In: (2010) (cit. on p. 3).
- [11] F. Plestan Y. Shtessel and M. Taleb. «Lyapunov design of adaptive super-twisting controller applied to a pneumatic actuator». In: (2011) (cit. on p. 3).
- [12] M. Taleb Y. Shtessel and F. Plestan. «A novel adaptive-gain supertwisting sliding mode controller: methodology and application». In: (2012) (cit. on p. 3).
- [13] V. I. Utkin and A. S. Poznyak. «Adaptive sliding mode control with application to super-twist algorithm: equivalent control method». In: (2008) (cit. on p. 3).

- [14] K. Lu and Y. Xia. «Finite-time attitude control for rigid spacecraft-based on adaptive super-twisting algorithm». In: (2014) (cit. on p. 3).
- [15] C.-C. Peng and C.-L. Chen. «Robust chaotic control of lorenz system by backstepping design». In: (2008) (cit. on p. 3).
- [16] L.-H. Chen and C.-C. Peng. «Extended backstepping sliding controller design for chattering attenuation and its application for servo motor control». In: (2017) (cit. on p. 3).
- [17] A. Levant. «Sliding order and sliding accuracy in sliding mode control». In: (1993) (cit. on p. 3).
- [18] J. A. Moreno and M. Osorio. «A lyapunov approach to secondorder sliding mode controllers and observers». In: (2008) (cit. on p. 3).
- [19] A. Benallegue L. Derafa and L. Fridman. «Super twisting control algorithm for the attitude tracking of a four rotors uav». In: (2012) (cit. on p. 3).
- [20] L. Derafa. «Quadcopter robust adaptive second order sliding mode control based on pid sliding surface». In: (2018) (cit. on p. 3).
- [21] A. Chalanga et al. «Implementation of super-twisting control: super-twisting and higher order sliding-mode observer-based approaches». In: (2016) (cit. on p. 3).
- [22] J. Huang M. Zhang and F. Chen. «Super twisting control algorithm for velocity control of mobile wheeled inverted pendulum systems». In: (2018) (cit. on p. 3).
- [23] Y.-R Li and C-Ch Peng. «Super-Twisting Sliding Mode Control Law Design for Attitude Tracking Task of a Spacecraft via Reaction Wheels». In: (2021) (cit. on p. 3).
- [24] R. Nadafi et al. «Super-twisting sliding mode control design based on Lyapunov criteria for attitude tracking control and vibration suppression of a flexible spacecraft». In: (2019) (cit. on p. 3).
- [25] J. T. Gravdahl O. Hegrenæs and P. Tondel. «Spacecraft Attitude Control Using Explicit Model Predictive Control». In: (2005) (cit. on p. 3).
- [26] J. Zhou Y. Guo and Y. Liu. «Distributed Lyapunov-Based Model Predictive Control for Collision Avoidance of Multi-Agent Formation». In: (2018) (cit. on p. 3).
- [27] D. M. Raimondo L. Magni and F. Allgöwer. «Nonlinear Model Predictive Control». In: (2009) (cit. on p. 3).
- [28] H. Park S. Di Cairano and I. Kolmanovsky. «Model Predictive Control Approach for Guidance of Spacecraft Rendezvous and Proximity Maneuvering». In: (2012) (cit. on p. 3).

- [29] C. Zagaris et al. «Model Predictive Control of Spacecraft Relative Motion with Convexified Keep-Out-Zone Constraints». In: (2018) (cit. on p. 3).
- [30] A. Bemporad and M. Morari. «Robust Model Predictive Control: A Survey». In: (1999) (cit. on p. 4).
- [31] M. Mammarella et al. «Attitude Control of a Small Spacecraft via Tube-Based Model Predictive Control». In: (2019) (cit. on p. 4).
- [32] M. Dentis and E. Capello. «Precise Attitude Control Techniques: Performance Analysis From Classical to Variable Structure Control». In: (2020) (cit. on pp. 4, 37, 38).
- [33] E. Capello. «Notes of the Course 'Dinamica e controllo dei veicoli spaziali' - Politecnico di Torino». In: (2021/2022) (cit. on pp. 8, 36, 84, 88).
- [34] C. Novara. «Notes of the Course 'Nonlinear control and aerospace applications' - Politecnico di Torino». In: (2022/2023) (cit. on p. 32).
- [35] W. Fehse. «Automated Rendezvous and Docking of Spacecraft». In: (2003) (cit. on pp. 34, 91–93).
- [36] G. Cook. «Satellite drag coefficients». In: (1965) (cit. on p. 37).
- [37] ECSS-E-HB-60-10A. «Space engineering - Control performance guidelines». In: (2010) (cit. on p. 42).
- [38] ESSB-HB-E-003 Working Group. «ESA pointing error engineering handbook». In: (2011) (cit. on p. 42).
- [39] F. Stesina. «Tracking Model Predictive Control for Docking Maneuvers of a CubeSat with a Big Spacecraft». In: (2021) (cit. on pp. 74, 76).
- [40] A. Bemporad. «Notes of the Course 'Model Predictive Control' - Politecnico di Torino». In: (2022/2023) (cit. on pp. 74, 76).
- [41] D. D. Mueller R. R. Bate and J. E. White. «Fundamentals of ASTRODYNAMICS». In: (1971) (cit. on p. 83).
- [42] G. Avanzini. «Notes of the Course 'Spacecraft Attitude Dynamics and Control' - Politecnico di Torino». In: (2008/2009) (cit. on pp. 85, 86, 89, 90).